Liquid-Phase Exfoliation and Applications of Pristine Two-Dimensional Transition Metal Dichalcogenides and Metal Diborides

by

Ahmed Yousaf

A Dissertation Presented in Partial Fulfillment
of the Requirements for the Degree
Doctor of Philosophy

Approved April 2018 by the
Graduate Supervisory Committee:

Alexander A. Green, Chair
Qing Hua Wang
Yan Liu

ARIZONA STATE UNIVERSITY

May 2018

ABSTRACT

Ultrasonication-mediated liquid-phase exfoliation has emerged as an efficient method for producing large quantities of two-dimensional materials such as graphene, boron nitride, and transition metal dichalcogenides. This thesis explores the use of this process to produce a new class of boron-rich, two-dimensional materials, namely metal diborides, and investigate their properties using bulk and nanoscale characterization methods. Metal diborides are a class of structurally related materials that contain hexagonal sheets of boron separated by metal atoms with applications in superconductivity, composites, ultra-high temperature ceramics and catalysis. To demonstrate the utility of these materials, chromium diboride was incorporated in polyvinyl alcohol as a structural reinforcing agent. These composites not only showed mechanical strength greater than the polymer itself, but also demonstrated superior reinforcing capability to previously well-known two-dimensional materials. Understanding their dispersion behavior and identifying a range of efficient dispersing solvents is an important step in identifying the most effective processing methods for the metal diborides. This was accomplished by subjecting metal diborides to ultrasonication in more than thirty different organic solvents and calculating their surface energy and Hansen solubility parameters. This thesis also explores the production and covalent modification of pristine, unlithiated molybdenum disulfide using ultrasonication-mediated exfoliation and subsequent diazonium functionalization. This approach allows a variety of functional groups to be tethered on the surface of molybdenum disulfide while preserving its semiconducting properties. The diazonium chemistry is further exploited to attach fluorescent proteins on its surface

making it amenable to future biological applications. Furthermore, a general approach for delivery of anticancer drugs using pristine two-dimensional materials is also detailed here. This can be achieved by using two-dimensional materials dispersed in a non-ionic and biocompatible polymer, as nanocarriers for delivering the anticancer drug doxorubicin. The potency of this supramolecular assembly for certain types of cancer cell lines can be improved by using folic-acid-conjugated polymer as a dispersing agent due to strong binding between folic acid present on the nanocarriers and folate receptors expressed on the cells. These results show that ultrasonication-mediated liquid-phase exfoliation is an effective method for facilitating the production and diverse application of pristine two-dimensional metal diborides and transition metal dichalcogenides.

DEDICATION

I dedicate this thesis to my parents for their unwavering support and love.

ACKNOWLEDGMENTS

I would like to thank the following people:

- My advisor Dr. Alexander A. Green for supervising my research, allowing me to explore different ideas, and supporting me throughout my journey in graduate school
- Our collaborator and one of my dissertation committee members, Dr. Qing Hua Wang for her support, guidance, and helpful discussions
- Dr. Yan Liu, member of my dissertation committee, for her time, and invaluable advice
- My undergraduate research advisors Dr. Basit Yameen and Dr. Ghayoor Abbas Chotana for introducing me to research
- Our lab manager Kristen Lee for helping out with all the HR work
- David Lowry and Shery Chang for teaching me how to use TEM
- All the members of Green and Wang labs with whom I had the pleasure of working, particularly Abhishek Debnath and Matthew Gilliam who worked closely with me on several projects
- Syed Muhammad Hassaan for helping me photograph my samples
- Saba Safdar for proof-reading my thesis
- And finally, all my friends who have been my support system for all these years in graduate school

TABLE OF CONTENTS

Page

CHAPTER Page

CHAPTER Page

CHAPTER Page

CHAPTER Page

LIST OF TABLES

Table Page

LIST OF FIGURES

Figure Page

Chapter 1

An Introduction to Two-Dimensional Metal Dichalcogenides and Metal Diborides

1.1. Graphene – The First Two-Dimensional Material

Graphene, a two-dimensional allotrope of carbon, consists of an atom-thick sheet of carbon atoms that are arranged in a hexagonal honeycomb lattice. In 2004, Geim and Novoselov reported the first technologically relevant synthesis of graphene and highlighted its semi-metallic nature.[1] Before this, low-dimensional materials, such as nanoparticles and carbon nanotubes were well-known, however, the existence of two-dimensional materials was only theoretically predicted,[2,3] or small traces of it were observed under electron microscopy. The intriguing structure of graphene combined with its unique electronic properties opened a floodgate into the field of two-dimensional materials. Since then, the thinnest material in the world has been shown to be 200 times stronger than steel, making it the strongest material known to humankind.[4] Electron mobility in graphene is 100 times greater than that in silicon and it can sustain current densities six orders of magnitude greater than that of copper.[5] Electrons in graphene have zero effective mass and can be described by a 2D analogue of Dirac's equation.[5] This allows relativistic quantum phenomena to be mimicked and investigated in tabletop experiments.[6] Geim and Novoselov received the Nobel Prize in Physics in 2010 for their contributions to the "groundbreaking experiments regarding the two-dimensional material graphene".

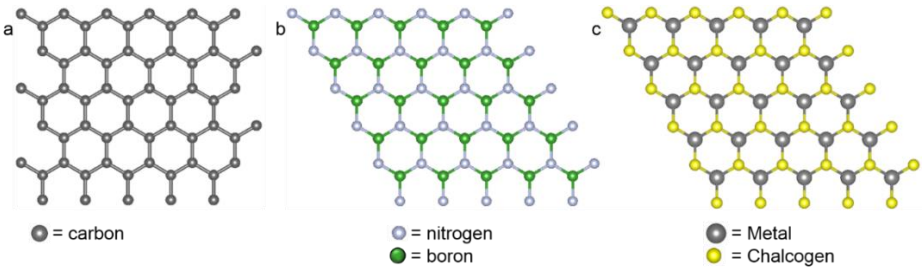

Figure 1.1 | Crystal structure of common two-dimensional materials. a, graphene **b**, boron nitride **c**, transition metal dichalcogenides.

Apart from the remarkable electronic and mechanical properties of graphene, its ultrathin anisotropic nature and an exceptionally high surface-area-to-volume ratio have made it a suitable candidate for various biological applications. Furthermore, it can be suspended in aqueous solutions to prepare stable dispersions, and its surface properties can be tuned by exploiting various covalent and non-covalent functionalization techniques. Several studies have established the biocompatibility of graphene and shown that it can be used as a vector to deliver cargo into cells.[7,8] Targeted drug delivery,[9,10] gene therapy,[11–13] bioimaging,[9,14] and biosensors[15,16] are among the various biological applications that graphene has been used for.

The synthesis of graphene, the two-dimensional carbon, inspired the production of many other materials with similar dimensionality. Silicene,[17] germanene,[18] stanene,[19] phosphorene,[20,21] and borophene,[22] which are the two-dimensional allotropes of silicon, tin, phosphorous, and boron, respectively, were produced in recent years. Apart from these, several two-dimensional compounds have also been synthesized, the most common of which are boron nitride (BN)[23], MXenes[24] and the transition metal dichalcogenides (TMDCs).[25] The wide array of two-dimensional materials, and the remarkably diverse set of properties that they possess, can lead to numerous applications which include, but are

not limited to, energy storage, superconductivity, filtration, photovoltaics, composite materials, semiconductor devices, and biosensing.[26–35]

1.2. Synthesis of Two-Dimensional Materials

Several methods have been used to synthesize two-dimensional materials. These methods can generally be divided into two categories: bottom-up synthesis and top-down exfoliation. The bottom-up approach is named so because it typically requires precursors that are reacted together in their molecular form to synthesize sheets of two-dimensional materials. The most common example of a bottom-up synthesis method is chemical vapor deposition. The top-down exfoliation involves the exfoliation of a bulk, three-dimensional layered material down to monolayer or few layer 2D sheets. Typical methods used for this are micromechanical exfoliation, ion-intercalation, and liquid-phase exfoliation. The methods, advantages, and drawbacks of all these techniques are briefly discussed in the following sections.

1.2.1. Micromechanical Exfoliation

The micromechanical exfoliation is a top-down approach and is commonly known as the scotch-tape method. It involves peeling off thin flakes of the bulk crystal and transferring them onto a substrate. These flakes can then be identified using light interference under an optical microscope. The method is conceptually simple, does not require any expensive or specialized equipment, and produces single-crystal flakes down to a monolayer with high purity. Geim and Novoselov used this approach to synthesize graphene for the first time.[1] Since then, this method has been applied to produce several two-dimensional materials such as MoS_2, WSe_2, BN, and phosphorene. Flakes produced

using this method are ideal samples for fundamental characterization of the materials and have been extensively used to make electronic and opto-electronic devices.[25] However, the method lacks scalability and control over size and thickness of flakes making it unsuitable for commercial production of two-dimensional materials.

1.2.2. Chemical Vapor Deposition (CVD)

Chemical Vapor Deposition is a bottom-up synthesis approach where vapors of one or more precursors decompose or react on the surface of a substrate to deposit a thin film of the desired material. Precursors can either be gaseous in nature or solid precursors that can be vaporized and then reacted in the vapor phase. The mechanism for the CVD process varies with the type of two-dimensional material being synthesized. For graphene, methane and hydrogen are reacted over a metal substrate and methane serves as the carbon source.[36] The type of metal substrate used in the case of graphene defines the mechanism. For copper substrate, graphene growth is a surface-catalyzed process in which methane dissociation is followed by diffusion of the carbon species on the surface, which leads to nucleation, island growth, and subsequent completion of the film.[37] However, when nickel is used the growth mechanism changes to a precipitation process, where after dissociation of methane the carbon diffuses into nickel and later forms graphene film upon segregation during the cooling process.[36] For TMDCs, typical growth processes are noncatalytic. MoS_2, for example, is grown using low-pressure CVD in which solid precursors, sulfur and molybdenum trioxide, are evaporated in a furnace and then co-deposited on a nearby substrate (Figure 1.2).[38]

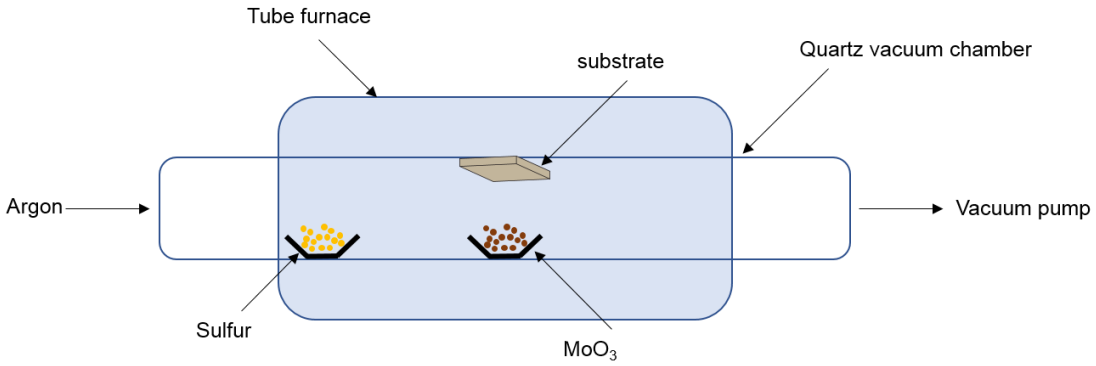

Figure 1.2 | CVD growth of MoS_2. Schematic showing the setup for CVD growth of MoS_2

CVD has the advantage that it can produce thickness controlled, large area sheets of two-dimensional materials with applications in electronics, and flexible and transparent optoelectronic devices.[25] Kobayashi et al. at Sony Corp. synthesized a 100 m long, high-quality graphene sheet using CVD which demonstrates the strength of the process.[39] The process, even though scalable, is limited by the compatibility of substrate and despite the availability of several methods to transfer CVD-grown films, the processing of these materials remains a challenge.

1.2.3. Ion Intercalation

Ion intercalation is a top-down approach where the bulk crystal of the source material is intercalated with metal ions, which causes swelling of the crystal, and weakens the interlayer forces.[40] This is followed by agitation of the mixture, for example by heating, which separates the sheets, and then excess ions are removed from the mixture to obtain a dispersion of the respective two-dimensional material. Typically, organolithium compounds are used for intercalation as the intercalated lithium ions, when exposed to water, react vigorously to produce hydrogen gas, which assists in rapid separation of the sheets. This method has been used to produce gram quantities of various

two-dimensional materials, including graphene[5] and MoS_2,[25,41] and the liquid-phase preparation makes it amenable to various processing methods, such as spray-coating and inkjet printing. However, two-dimensional materials produced using ion-intercalation method differ structurally and electronically from their source material. For example, when MoS_2 is exfoliated using ion-intercalation, coordination around the Mo atom changes from trigonal prismatic (2H-MoS_2) to octahedral (1T- MoS_2), and it goes from being a semiconductor to a metallic conductor,[25] thereby significantly affecting the application of the material.

1.2.4. Ultrasonication-assisted exfoliation

To avoid changes in chemical and electronic properties of the nanomaterial while maintaining the advantages of liquid-phase exfoliation, direct ultrasonication of bulk material in organic solvents or aqueous surfactant solutions can be used.[40,42,43] Ultrasonication, or simply sonication, is a process in which sound energy, typically ultrasonic, is applied to a sample either through a bath sonicator or a sonication probe. The use of high-amplitude sound waves forms cavities or tiny bubbles in the liquid. Upon continuous application of ultrasonic waves, these bubbles implode giving off a burst of energy, which is then used for exfoliation. This collapse of bubbles can either occur on the surface of the material, which causes direct damage, or in the liquid, which results in a high-speed microjet that hits the solid material. This energy can cause two phenomena to occur: the exfoliation of the material, and the fragmentation of the crystal (or scission). Scission, undesirable in many cases, is unavoidable and leads to smaller flakes.[25]

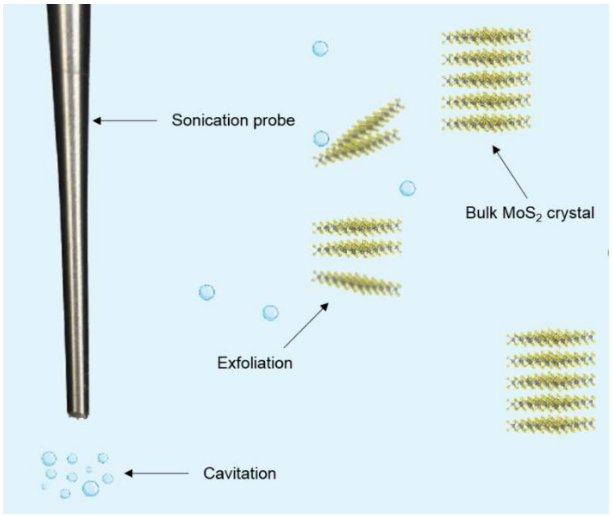

Figure 1.3 | Liquid-phase exfoliation. Schematic diagram showing ultrasonication-assisted exfoliation of MoS_2.

Once the material is exfoliated, the organic solvent molecules, or the surfactant molecules in case of an aqueous dispersion, stabilize the nanosheets, and prevent reaggregation. The case of aqueous, surfactant-based dispersion is explained by the Derjaguin – Landau – Verwey – Overbeek (DLVO) theory,[44] which describes the balance between Van der Waals and electrostatic repulsion forces as the key factor to determine stability of a colloidal dispersion. However, in case of organic solvent-based dispersions, there are almost no electrostatic forces present. This means that the interaction between nanosheets and solvent molecules is stronger than the interlayer forces present between the sheets of the bulk crystal. It has been shown that three forces primarily govern this interaction: hydrogen bonding, dipole-dipole, and dispersion forces. Hansen and Hildebrand solubility parameters of graphene,[45] MoS_2 and several other two-dimensional materials[46] were determined to understand the nanomaterial-solvent interaction. A detailed discussion on the solubility parameters is presented in a later section.

Ultrasonication does not allow good control over the size and thickness of flakes, however, the ability to produce large quantities of pristine two-dimensional materials dispersed in liquid makes it quite useful. Methods, such as density gradient ultracentrifugation (DGU), can further be used to enrich the dispersions in flakes of a particular thickness or size if necessary.[46] These dispersions can be used in making coatings and thin films, composites, and hybrids of different materials by simple mixing.

1.3. Characterization Techniques for Two-Dimensional Materials

Two-dimensional materials can be characterized using a wide array of techniques. One of the most fundamental characterizations for these materials is determining their dimensionality. The most common tools used for this are optical microscopy, atomic force microscopy (AFM), transmission electron microscopy (TEM), and Raman spectroscopy. Flakes produced using micromechanical exfoliation are typically detected using optical microscopy first. This method depends on changes in optical path lengths with different thicknesses which can be identified under an optical microscope by a well-trained eye. Usually, the material is exfoliated on silicon wafer with a thin silica layer and the thickness of this silica capping layer also affects the contrast in the image. The contrast can be further improved by using monochromatic light for imaging. Figure 1.4 shows a micromechanically cleaved MoS_2 sample where monolayer MoS_2 can be identified solely through the difference in contrast. The AFM image was collected by Ximo S. Chu.

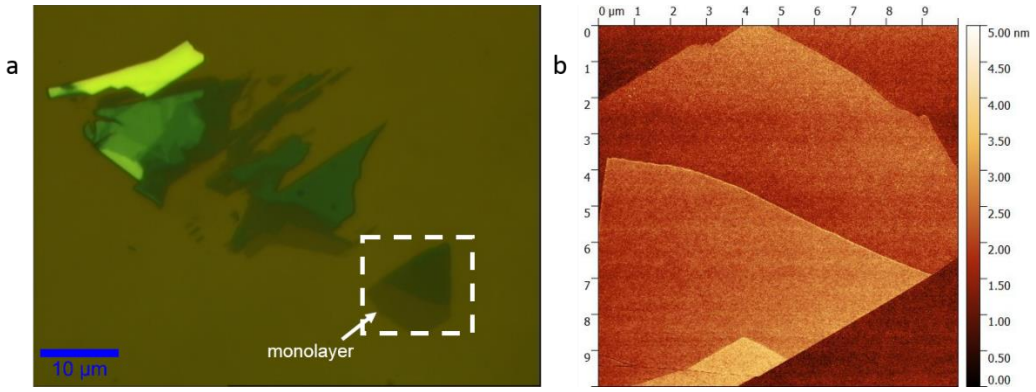

Figure 1.4 | Identification of monolayers. a, optical microscopy image of micromechanically exfoliated MoS_2. The arrow indicates the monolayer. **b**, AFM image of the MoS_2 flake boxed in 3a.

AFM is used to get the thickness of the flakes and determine their topography. Monolayer graphene is 0.34 nm thick and can appear to be almost 1 nm in thickness under AFM, due to the interaction of the tip of AFM with the water adsorbed on the surface of the flake. Figure 1.4 shows an exfoliated MoS_2 flake, the one boxed in figure a, where the arrow indicates the monolayer part of the flake with a thickness of ~0.5 nm and one edge is folded over.

For liquid-phase exfoliation, the nanosheets are dispersed in a liquid and can easily be imaged using TEM, which makes it the basic characterization tool used to determine their morphology. High-resolution TEM (HRTEM) is also extensively used to study the crystal structure of two-dimensional materials. The colloidal nature of the nanosheets simplifies the sample preparation as it can simply be dropped onto the TEM grid and imaged directly. Figures 1.5a and 1.5b show TEM images of MoS_2 and $MoSe_2$ dispersed in different aqueous surfactant solutions and figure 1.5c shows an HRTEM image of $MoSe_2$ dispersed in DNA.

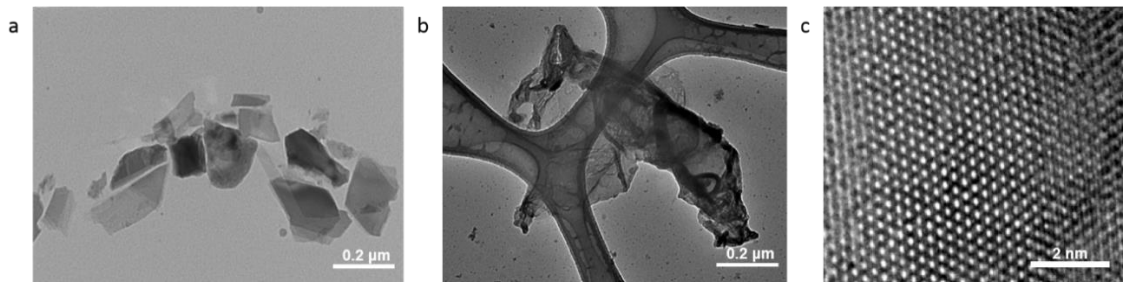

Figure 1.5 | TEM images of two-dimensional materials. a, MoS_2 dispersed in tetronic 1104. **b**, $MoSe_2$ in F68.**c**, HRTEM image of $MoSe_2$ dispersed in DNA. The hexagonal crystal structure can easily be observed from this image.

Nanosheets that are prepared by micromechanical cleavage or grown using CVD on a substrate must be transferred onto a TEM grid using multiple steps. Typically, a polymer such as polydimethylsiloxane (PDMS) or polymethyl methacrylate (PMMA), is spin-coated on the sample and then the substrate is dissolved using an etchant.[47] Finally, the sample is transferred face-down onto the grid and the polymer is dissolved using a solvent. This step tends to leave behind a lot of residue which can be problematic while doing high-resolution TEM imaging. Furthermore, the TEM grids are quite delicate, and can get damaged in the process.

Raman spectroscopy is also extensively used for characterizing two-dimensional materials. It is a type of vibrational spectroscopy that relies on inelastic scattering (or Raman scattering) of light to provide a structural fingerprint of a molecule. For two-dimensional materials, apart from identification this technique can be used to determine the number of layers in most cases. For graphene, the peak position for G band shifts with the layer number and the ratio of G and 2D peak intensities increases with the layer number.[47]

Further chemical characterization can be carried out using x-ray photoelectron spectroscopy (XPS), energy dispersive x-ray spectroscopy (EDS), and electron energy

loss spectroscopy (EELS). XPS is a surface technique that works on the principle of photoelectric effect. Briefly, the material is exposed to high energy x-rays which knock out the inner shell electrons of the atoms and the energy of the emitted electron is detected. This can be used to calculate the binding energy (B.E.) of the emitted electrons. The number of electrons is plotted against the binding energy and the peak position, and relative intensities of the peaks help in identifying the elements, the chemical state of those elements, and the relative composition of the constituents on the surface.

$$B.E. = h\upsilon - (K.E. + \emptyset)$$

Here hυ is the energy of the x-rays, K.E. is the kinetic energy of the emitted electrons and $\emptyset$ is the work function that depends on both the material and the spectrometer.

EDS is a qualitative or semi-quantitative technique that is commonly used for elemental analysis. In EDS, the material is bombarded with high energy x-rays or electrons that remove a core electron from the atom leaving an electron hole behind. The hole is filled by an electron from a higher energy level and this transition gives off energy, typically in the x-ray range, which is then detected. The energy of the emitted x-rays is representative of the difference between energy levels of the element and thus, allow its identification.

EELS, on the other hand, is a quantitative technique that not only helps identify the elements present in the material but also allows the measurement of the relative ratio in which they are present. In EELS, the sample is exposed to an electron beam of known energy. As the electrons pass through the sample, they undergo inelastic scattering and hence, lose some energy in the process. The inelastic scattering can occur for several

reasons but most important is the inner shell ionization. This loss in energy can be detected by an electron spectrometer and is used to calculate the relative ratio and identity of the elements present. EDS and EELS are complementary techniques as EDS is quite useful for heavier elements, whereas EELS is more commonly used for identifying lighter elements. However, the quantitative nature of EELS, its ability to identify chemical bonding environment, and calculate the band structure of the material being studied sets it apart from EDS.

1.4. Transition Metal Dichalcogenides

Transition metal dichalcogenides (TMDCs) are a family of layered materials with the general formula MX_2, where M is a transition metal and X is a chalcogen. The most common TMDCs are MoS_2, $MoSe_2$, WS_2, WSe_2, and WTe_2. The structure of TMDCs consists of layers of chalcogen atoms arranged in a hexagonal lattice with metal atoms sandwiched between them and the adjacent layers are stacked one on top of the other via weak van der Waals forces as shown in Figure 1.6. The central metal atom either has octahedral or trigonal prismatic coordination and the overall symmetry of the crystal can either be hexagonal or rhombohedral resulting in a variety of polytypes. Similar to graphene, the weak van der Waals forces present between the sheets allow their exfoliation from their bulk state to their two-dimensional form.

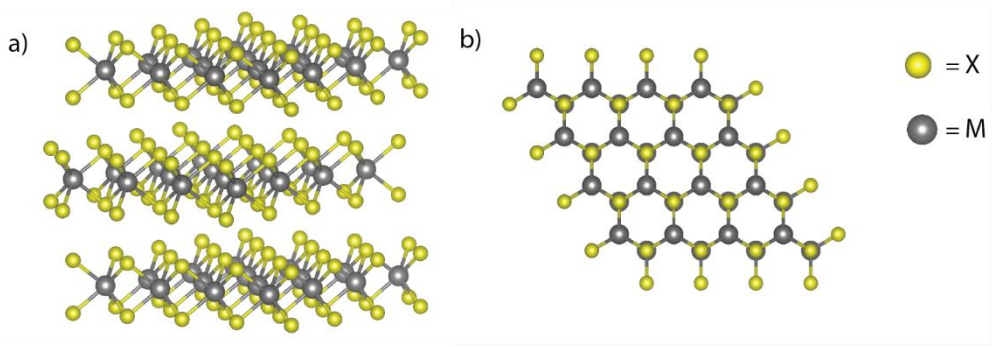

Figure 1.6 | Crystal structure of transition metal dichalcogenides. a, Sideview of TMDC structure. **b**, top view of TMDC structure.

The exfoliation or synthesis of two-dimensional TMDCs (2D-TMDCs) has generated a great deal of interest due to their exceptional electronic and optoelectronic properties. MoS_2, $MoSe_2$, WS_2, and WSe_2 are well-known semiconductors, whereas NbS_2, $NbSe_2$, TaS_2 and $TaSe_2$ are superconducting.[25] Furthermore, TMDCs possess layer-dependent properties. MoS_2, the archetypal TMDC, is an indirect bandgap semiconductor in bulk form, whereas single-layer MoS_2 is a direct bandgap semiconductor. Not only that, going from bulk to monolayer forms, the bandgap of MoS_2 increases from 1.3 eV to 1.9 eV and shows photoluminescence (PL).[48]

1.4.1. Applications in Electronic and Optoelectronic Devices

TMDCs in Transistors. 2D-TMDCs, such as MoS_2, are promising materials for use in field-effect transistors (FETs). An FET consists of a source and drain terminal that are connected by a semiconducting channel and a gate terminal that modulates the conductivity of the channel. For decades, silicon has been used as the semiconducting channel material in industry, however, silicon-based FETs are reaching the limit of scalability as the current transistors hit a feature length of 10 nm.[49] Typical properties desired in a transistor are high on/off ratio, charge-carrier mobility, conductivity, and low

off-state conductance.[25] Unlike graphene, TMDCs possess an intrinsic bandgap and can be used to make FETs with high on/off ratio. Furthermore, the ultrathin nature of TMDCs can help overcome the issues with miniaturization by reducing the key limiting factors of power dissipation and short channel effects.[50]

In 2011, Radisavljevic et al. demonstrated that monolayer MoS_2 FET with HfO_2 gate dielectric showed electron mobilities as high as 200 $cm^2 V^{-1} s^{-1}$, on/off ratio in the order of 10^8 at room temperature and ultralow power dissipation.[50] Later, Wang et al. reported integrated circuits based on monolayer MoS_2 that can perform digital logic operations.[51] Qiu et al. used bilayer MoS_2 to build a high-performance FET and studied the effects of adsorption of oxygen and moisture on the performance of the FET under ambient conditions.[52] Liu et al. showed that few-layer MoS_2 FETs show smaller contact resistance and higher electron mobilities as compared to their monolayer and bilayer counterparts.[53] In addition to MoS_2, several other TMDCs including $MoSe_2$,[54] WS_2,[55] and WSe_2[56] have been used to build high-performance FETs.

TMDCs in Optoelectronic Devices. Ultrathin TMDCs with direct bandgaps in the visible region of the electromagnetic spectrum, are promising materials for thin-film solar cells, flexible photovoltaics, light emitting diodes (LEDs), and display panels. The basic component of an optoelectronic device is a p-n junction diode. Using TMDCs, a p-n diode can be built by making its heterojunctions with commonly used semiconductors, such as silicon or by making van der Waals heterostructures of TMDCs. A typical van der Waals heterostructure has two or more two-dimensional materials, which are stacked vertically and display remarkable new properties due to quantum coupling. Tsai et al.

fabricated a solar cell by forming a heterojunction between MoS_2 and p-type silicon, which could achieve a power conversion efficiency greater than 5%.[32] Gong et al. developed a one-step route to produce vertically stacked heterostructures of WS_2 and MoS_2, which display strong PL and generate a p-n junction.[57] Hong et al. used PL mapping and femtosecond pump-probe spectroscopy to observe the charge-transfer process in MoS_2-WS_2 heterostructures.[58] They showed that hole-transfer between MoS_2-WS_2 heterojunction occurs within 50 fs after optical excitation.

Pospischil et al. demonstrated solar energy conversion in a p-n diode made from electrostatically doped WSe_2 monolayer.[59] They showed applications in LEDs, photodiodes, and photovoltaic solar cells. Cheng et al. built a p-n diode by making a heterostructure of WSe_2 and MoS_2, which can generate photocurrent with remarkable current rectification and show electroluminescence.[60] Choi et al. studied photogeneration and wide-spectrum photo-response in phototransistors made from multilayer MoS_2.[61] Their work suggests that MoS_2-based phototransistors can be incorporated into a variety of optical sensors. All of the above-mentioned examples establish TMDCs as promising materials for use in various optoelectronic devices.

1.4.2. Biological applications of TMDCs

2D-TMDCs, by nature, are ultrathin anisotropic materials, and have dimensions proportionate to critical length scales in biology. Their extreme thinness results in an exceptionally high surface to volume ratio and makes them immensely sensitive to external stimuli. Several TMDCs show photoluminescence, are known to be stable in an aqueous environment, and possess surface properties that can be tuned using covalent and

non-covalent functionalization techniques.[61] Furthermore, several studies have been carried out that suggest a low toxicity for 2D-TMDCs[62] and explore the mechanism of their biodegradability.[62] Combining these properties make them attractive candidates for various biological applications, such as drug delivery, biosensing, and cell-labeling.

Lithium-intercalated MoS_2 and WS_2 have been explored for cancer treatment, either via photothermal therapy[63,64] or a combination of photothermal and photodynamic therapies.[65–67] Other combination therapies incorporating multimodal bioimaging techniques with photothermal ablation or chemotherapy are also reported. For example, Liu et al. used iron-oxide decorated Li-MoS_2 for multimodal imaging and photothermal therapy[68] and Kim et al. explored Li-MoS_2 composites with polyethylene imine (PEI) and polyethylene glycol (PEG) as non-viral vectors for stimuli responsive gene delivery.[69]

1.5. Metal Diborides

Metal diborides (MB_2) are a class of layered materials that contain vertically stacked hexagonal boron sheets of graphene-like structure, with metal atoms sandwiched between the sheets as shown in Figure 1.7. Every metal atom is surrounded by 12 equidistant boron atoms which are present in the planes above and below the metal layer, and 6 metal atoms in the same plane.[70]

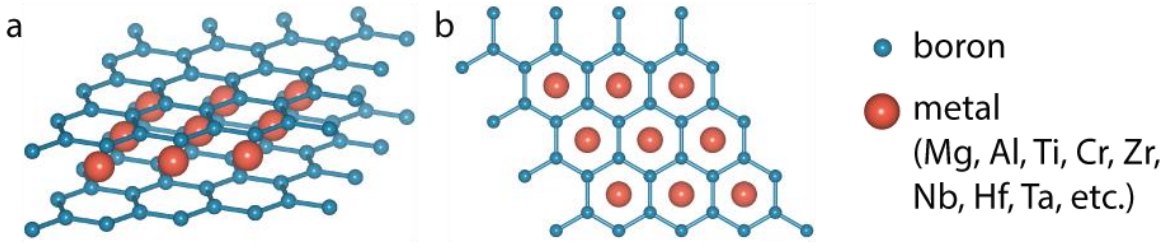

Figure 1.7 | Crystal structure of metal diborides. **a**, Sideview of the metal diboride structure showing layers of boron and metal atoms. **b**, Top view of the metal diboride structure.

1.5.1. Bonding in Metal Diborides

The nature of bonding present between the alternating metal and boron layers is very different from previously discussed van der Waals solids, such as graphite and TMDCs. In case of van der Waals solids, there are strong covalent bonds present between atoms in the individual layers, and these individual layers are held together by weak van der Waals forces.[40] The case of MB_2 is more complex as they possess mixed bonding characteristics. For diborides of main group elements, such as magnesium and aluminum, the nature of bonding between the metal-boron layers is predominantly ionic, which arises due to the electron transfer from metal to boron atoms.[71] Within the boron layer, covalent bond is present, however, the atoms in the metal layer have negligible metallic bonding. In contrast, in transition metal diborides, such as hafnium and zirconium, the nature of bonding between the metal-boron layers is a mixture of covalent and ionic. Apart from the electron transfer from metal to boron layer, the partial interaction of *d*-electrons of metals with *p*-electrons of boron imparts the covalent character to the metal-boron bond leading to a more complex bonding environment.[72] The atoms in the boron layer are covalently bonded, and the ones in the metal layers have bonds with both metallic and covalent characteristics.

1.5.2. Applications of Metal Diborides

MB_2 have attracted considerable attention over the years due to their remarkable physical and chemical properties such as hardness, thermal conductivity, and high melting temperatures. With every metal comes a different set of properties: MgB_2 is a well-known superconductor at 39 K;[73] TiB_2 has a very high melting temperature and

shows electrical conductivity higher than the titanium metal itself;[74] ZrB_2 and HfB_2 are ultra-high temperature ceramics (UHTCs)[75] with applications in aerospace industry, such as building components of atmosphere reentry vehicles; and ReB_2 and OsB_2,[76] which contain puckered boron sheets instead of planar sheets, are ultrahard materials with Vickers hardness over 40 GPa,[77] which is the limit for ultrahard materials.

1.5.3. Towards Exfoliation of Layered Boron Materials

Two-dimensional boron compounds such as borophene have been theoretically shown to possess remarkable electronic and mechanical properties.[78] The first experimental realization of two-dimensional boron was reported by Mannix. They used physical vapor deposition (PVD) in ultra-high vacuum at high temperatures to produce an atom-thin sheet of boron with rectangular symmetry.[22] The puckered boron sheet was grown on silver and was unstable in environmental conditions. They also used Scanning Tunneling Spectroscopy (STS) to confirm theoretical predictions of metallic characteristics of borophene. Feng et al. also synthesized borophene via epitaxial growth on a silver substrate.[79] Since then several theoretical studies have predicted two-dimensional boron as a promising electrode material for batteries, and nano-superconducting devices.[79]

Alongside borophene, several attempts have been made to synthesize two-dimensional sheets of structurally similar metal diborides but have seen limited success. Das et al. produced chemically modified MgB_2 by sonicating bulk MgB_2 powder in water.[80] The same group also reported a chelation-assisted strategy to produce boron-based nanosheets from MgB_2.[81]

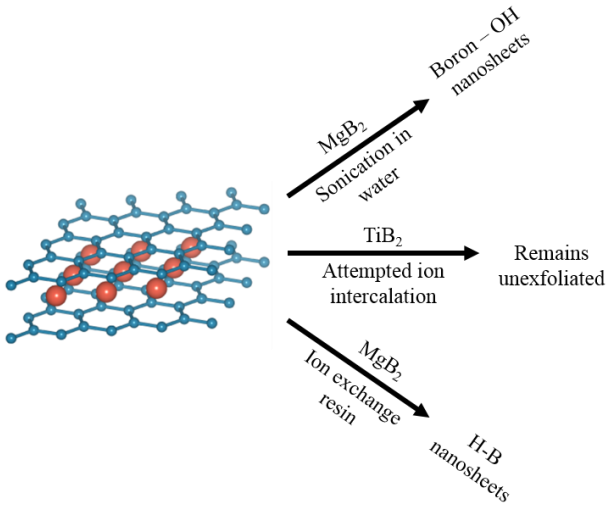

Figure 1.8 | Attempted exfoliation of Metal Diborides. Schematic showing different exfoliation strategies previously employed for attempted exfoliation of metal diborides.

Nishino et al. showed that sonication of MgB_2 in water produces highly functionalized boron nanosheets that have hydroxyl groups on the surface and are Mg-deficient.[82] They also produced hydrogen boride (HB) by reacting MgB_2 with an ion exchange resin in an aqueous solution.[83] Lim et al. treated TiB_2 with butyllithium and sodium naphthalinide but were unsuccessful in its exfoliation.[84]

1.6. Thesis Organization

In this thesis, I will describe how liquid-phase exfoliation can be used to produce bulk dispersions of a new class of two-dimensional boron-rich materials. I will further show how liquid-phase methods can be used to synthesize and functionalize pristine two-dimensional TMDCs and that the dispersions produced as such can be used in applications such as targeted drug delivery.

In Chapter 2, I present a method to exfoliate a new class of two-dimensional materials, the metal diborides, their complete characterization, and their application in

polymer reinforcement. These liquid-phase dispersions of metal diborides also provide an alternative route to easy processing of the ceramic diborides materials.

In Chapter 3, I discuss the effect of the choice of solvent on dispersing metal diborides and the parameters that should be considered when making that choice. The Hansen and Hildebrand solubility parameters are calculated for three of the 2D-MB_2 and the relationship between the surface energy of solvent and the diboride is also studied.

In chapter 4, I describe a method to functionalize pristine, liquid-dispersed MoS_2 using diazonium chemistry. A material interacts with its environment through its surface, and if we can control the surface properties of a material we can tune that interaction and define many of its applications. For MoS_2, I show that we can use this chemistry to attach functional molecules on the surface with potential applications in chemical and bio-sensing.

In Chapter 5, I detail how liquid-dispersed pristine two-dimensional materials can be used to deliver anticancer drugs to cells *in vitro*. This method is generalizable and can be applied to a variety of two-dimensional materials for drug loading, delivery and targeting.

In Chapter 6, I conclude my thesis by presenting a summary of the work and discuss what future directions can be explored based on this work.

Chapter 2

Solution-Phase Production of Two-Dimensional Metal Diborides and Their Application in Polymer Reinforcement

2.1. Abstract

Liquid-phase exfoliation has been established as an efficient process for bulk production of two-dimensional (2D) materials such as graphene, transition metal dichalcogenides, and phosphorene. Borophene, a 2D material containing planar boron, has recently been shown to possess exceptional electronic properties and theoretically predicted outstanding mechanical properties. However, the challenging synthesis and the environmental instability of borophene limit its use outside the laboratory. Here we demonstrate the production of a new class of boron-based 2D materials, the metal diborides, which contain planar hexagonal boron sheets analogous to graphene separated by metal atoms, through liquid-phase exfoliation of bulk metal diborides. Atomic- and bulk-scale characterization elucidate the structure, composition, and dispersion properties of the nanosheets. We also demonstrate the remarkable ability of as-exfoliated chromium boridene to be incorporated directly into polymers for mechanical reinforcement, increasing the elastic modulus and the ultimate tensile strength by 94% and 100%, respectively. These improvements in mechanical strength exceed those of the other directly exfoliated 2D materials BN, MoS_2, and graphene; and are matched only by graphene after it has been subjected to size sorting. The ease and scalability of this method for producing high-concentration dispersions of various metal boridenes, each with a set of potentially unique properties, suggests future uses in structural applications

and also opens up new, low-temperature processing methods for the metal diborides in their conventional applications in aerospace, armor, and superconducting cables.

2.2. Introduction

Allotropes of boron, the fifth element in the periodic table, are considered companion compounds of carbon allotropes and have attracted considerable interest as a result of their exceptional electrical and mechanical properties[22,79]. Despite these properties, synthesis of large quantities of low-dimensional boron compounds has remained a significant challenge. Theoretical and experimental observation of boron clusters of various structures[85], single-walled boron nanotubes[86] and borospherene[87], the boron analogue of buckminsterfullerene, are important discoveries in this field. Multiple theoretical studies have also suggested the existence of stable borophene[88,89,90], the boron analogue of graphene, and predicted its metallic nature[78]. Recently, Mannix et al. successfully synthesized borophene on a Ag(111) substrate in ultra-high vacuum (UHV) using a solid boron atomic source, revealing a two-dimensional material with a buckled structure and rectangular crystal lattice[22]. In another work, Feng et al. used molecular beam epitaxy to grow borophene on a Ag(111) substrate in UHV[79], observing planar boron sheets in triangular lattices with periodic holes. Both these methods of synthesizing borophene, however, yield low quantities of material and require both UHV and high temperature conditions. As a result, two-dimensional boron allotropes have yet to be produced in bulk form, and their properties have not been characterized beyond the atomic scale.

Liquid-phase exfoliation has emerged as an attractive method to produce bulk quantities of high quality two-dimensional materials[21,40,91,92]. By subjecting inexpensive powder forms of layered materials to ultrasonic waves in organic solvents or aqueous surfactant solutions enables atomically thin sheets of compounds such as graphene[93] and transition metal dichalcogenides[94] (TMDCs) to be stably dispersed at concentrations greater than 10 mg/mL. Nanosheets of 2D materials from these solution-phase dispersions can then be readily exploited in applications such as reinforced plastics[34,95], field-effect transistors[50], supercapacitors[96], hydrogen production systems[97] and batteries[28]. However, efforts to produce two-dimensional boron compounds using liquid-phase approaches have thus far been unsuccessful. Unlike the other 2D materials that can be produced by liquid-phase exfoliation, borophene cannot directly be exfoliated from a layered powder because boron does not exist in bulk form as a layered material. Moreover, attempts at exfoliation of compounds containing boron layers have thus far had limited success: a chemically modified form of MgB_2 has been produced in water[80], in which MgB_2 readily undergoes oxidation[98] and TiB_2 was treated with sodium naphtalenide and butyllithium but was not successfully exfoliated[84].

Herein, we report the first stable, high-concentration liquid-phase dispersions of two-dimensional boron sheets in both aqueous solutions and organic solvents. The source materials for these two-dimensional sheets are inexpensive powders of the family of boron-rich materials known as metal diborides. They have the common chemical formula MB_2, where M is a metal. Metal diborides possess a layered structure containing hexagonal sheets of boron with metal atoms sandwiched between them (Figure 2.1a).

We demonstrate that stable high-concentration dispersions can be produced from eight different metal diboride sources via sonication in aqueous solution or organic solvents. The resulting two-dimensional metal diborides, with composition and structural similarities to graphene, are characterized in detail using transmission electron microscopy (TEM), atomic force microscopy (AFM), scanning tunneling microscopy (STM), electron energy loss spectroscopy (EELS), inductively coupled plasma mass spectroscopy (ICP-MS), and optical absorbance spectroscopy (UV-Vis). These measurements confirm the two-dimensional nature of metal diborides and the retention of their hexagonal structure after exfoliation. Furthermore, they also show that the chemical composition is not affected by the sonication process and results in little to no oxidation.

In addition, we also demonstrate that chromium diboride can be directly dispersed in aqueous solutions of polymers such as polyvinyl alcohol (PVA) and used to make mechanically reinforced metal diboride-PVA composites. The resulting polymer composites provide substantial improvements in elastic modulus and ultimate tensile strength of 94% and 100%, respectively. These figures of merit for the diboride-polymer composites exceed those obtained from sheets of other 2D materials such as graphene[34], MoS_2[94], and boron nitride[95] even after they have been subjected to time-consuming size-sorting procedures to select for the largest nanosheets.

Overall, these results reveal a new class of 2D boron materials with novel mechanical properties and open up the family of metal diborides to solution-phase processing amenable to their use in flexible and stretchable forms. These materials are also unique in the sense that they, like traditional two-dimensional materials, do not

possess weak interlayer Van der Waals forces, rather it has been shown that metal diborides exhibit a strong interlayer bonding which has been described as a mixture of ionic and covalent bonding between the metal and boron atoms[70,99]. Furthermore, our method also provides an alternative route for cheap, room temperature processing of bulk metal diboride materials which would otherwise require high-temperature treatment, making it an attractive candidate for colloidal processing of ceramics.

2.3. Results

2.3.1. Exfoliation of MB_2

Few-layer metal diboride sheets were prepared using ultrasonication in a variety of solvents and aqueous surfactant solutions (Figure 2.1b). Ultrasonication relies on the principle of cavitation to shear apart the sheets, which are then stabilized by the surrounding solvent or surfactant molecules. The process involved sonicating 0.4 g of each bulk metal diboride powder in 6 mL of each solvent or surfactant solution at a suitable power (11-13 W) for one hour. Following centrifugation to remove poorly dispersed materials, the supernatant was decanted. This process was applied to eight different metal diborides: magnesium diboride (MgB_2), aluminum diboride (AlB_2), titanium diboride (TiB_2), chromium diboride (CrB_2), zirconium diboride (ZrB_2), niobium diboride (NbB_2), hafnium diboride (HfB_2), and tantalum diboride (TaB_2). The resulting solution-phase dispersions were grey to dark black depending on the metal diboride and remained in suspension for weeks without precipitating with the exception of AlB_2, which precipitates after 2-3 days. Figure 2.1e shows a photograph of dispersions of the different metal diboride prepared using this method. The optical absorbance spectra

obtained from the dispersions are mostly featureless with the exception of MgB_2, which shows two broad peaks near 400 nm and 850 nm as shown in Figure 2.1d. Dimethylformamide (DMF) was found to be an effective solvent for MgB_2 and AlB_2, while N-methyl-2-pyrolidone (NMP) was effective for HfB_2 and TaB_2. TiB_2 and CrB_2 were efficiently dispersed in aqueous solution using the anionic surfactant sodium cholate (SC) and ZrB_2 and NbB_2 were best exfoliated in aqueous solution using the cationic surfactant myristyltrimethylammonium bromide (MTAB).

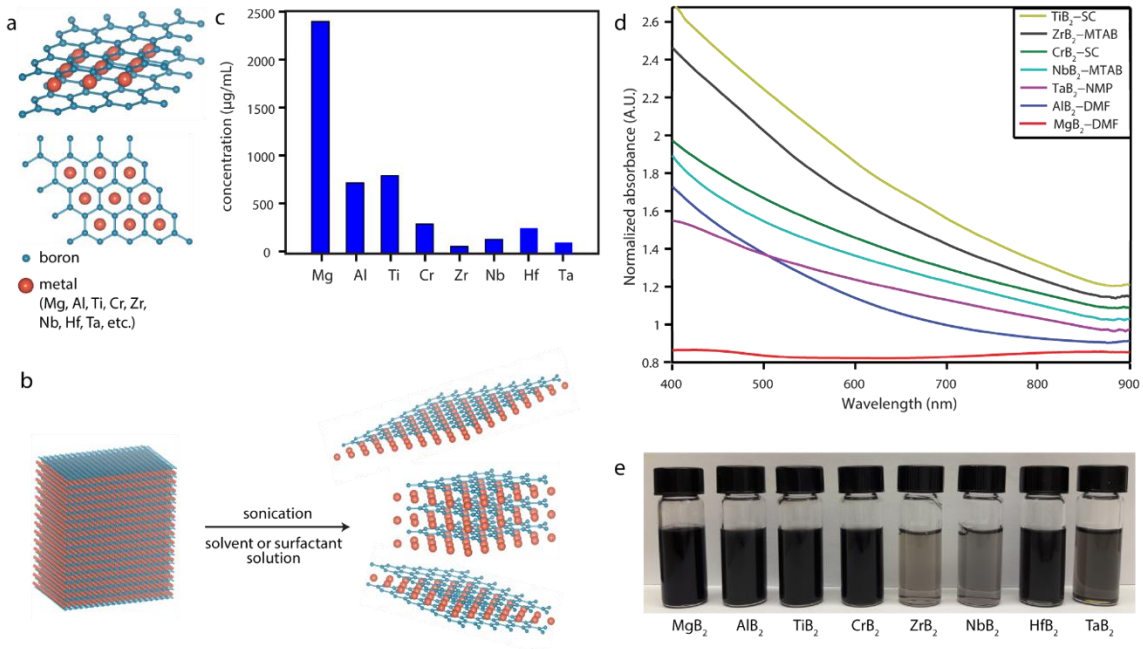

Figure 2.1 | Solution-phase production of 2D metal diborides. a, Crystal structure of metal diborides consisting of boron layers separated by metal atoms. **b**, Schematic of the exfoliation process employed to disperse the metal diborides. **c**, Concentrations of the metal diborides as determined from ICP-MS. **d**, Optical absorbance spectra of eight metal diboride dispersions. Curves have been offset for clarity. **e**, Photograph of the metal diboride dispersions in organic solvents and aqueous surfactant solutions.

The concentrations of the metal diboride liquid-phase dispersions were determined using ICP-MS. These measurements showed a broad range of concentrations from a high concentration of 2.4 mg/mL for MgB_2 to a low concentration of 0.07 mg/mL

for ZrB_2 (Figure 2.1c). These values are comparable to the concentrations reported for initial studies of the most widely studied 2D materials, such as graphene, BN, and TMDCs[43,100]. Khan et al. prepared graphene dispersions in NMP with a concentration of 1.2 mg/mL using long sonication times[101]. Smith et al. studied surfactant stabilized dispersions of MoS_2, WS_2, $MoSe_2$, $MoTe_2$, $NbSe_2$, $TaSe_2$ and BN with concentrations varying from 0.25 mg/mL to 0.5 mg/mL depending on the initial surfactant concentration and sonication time[42].

2.3.2. Structural characterization of MB_2

To confirm the 2D nature of the sheets, low-resolution TEM images were obtained for all eight metal diborides (Figure 2.2a-2.2h). The flakes are found in different morphologies varying from flat, planar sheets, as shown for the MgB_2, AlB_2, TiB_2, and CrB_2, to folded and crumpled ones, as shown for ZrB_2, NbB_2, HfB_2 and TaB_2. The flake sizes were found to vary, with AlB_2 possessing the smallest flakes (< 100 nm) and MgB_2 having the largest flakes reaching up to several microns in size.

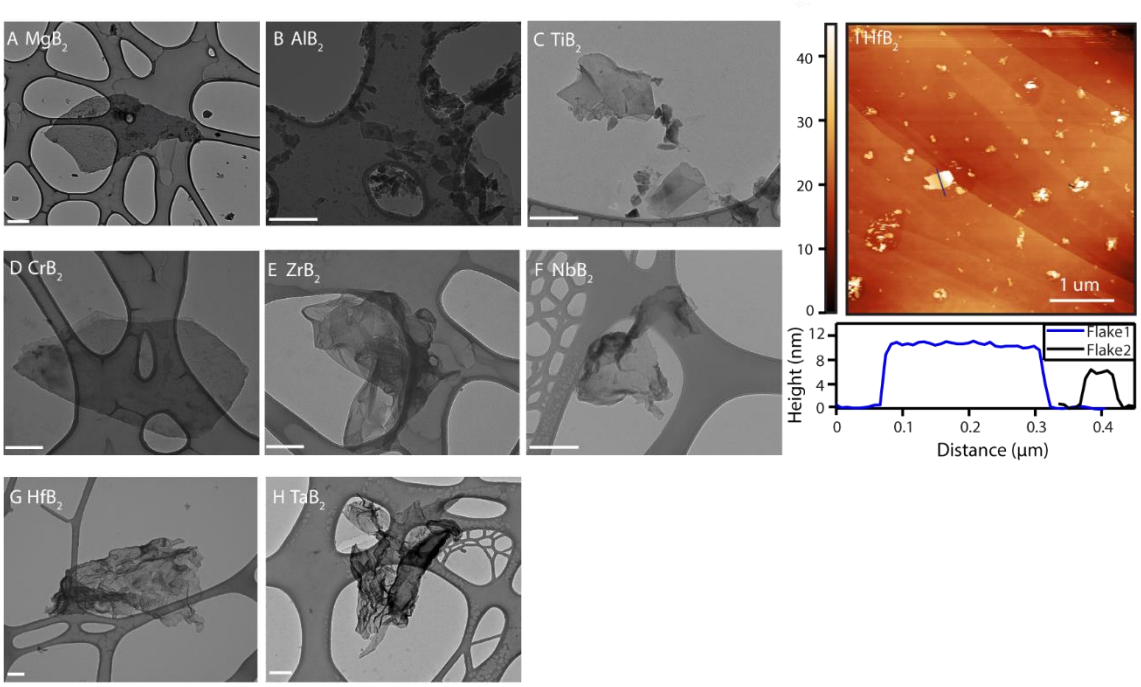

Figure 2.2 | TEM and AFM imaging of 2D metal diborides. a-h, Low magnification TEM images of eight different metal diborides displaying lateral dimensions ranging from 30 nm to 2 μm and planar or crumpled morphologies. Scale bar is 200 nm. **i**, AFM image of hafnium diboride deposited onto a SiO_2/Si wafer with flakes 30 nm to 500 nm in lateral extent and thicknesses of 6 nm or higher. **j**, Height profile of two metal diboride nanosheets from panel i.

Nanosheets of HfB_2 were deposited onto an HOPG substrate and imaged using AFM (Figure 2.2i). These measurements showed flakes of different sizes and varying thicknesses. Height profiles of two flakes are shown in Figure 2.2j, revealing the planar structure and thicknesses of 6 nm and 11 nm. Given the interlayer spacing of 0.35 nm for crystalline HfB_2, these thicknesses correspond to nanosheets consisting of 10 to 20 boron layers. Careful analysis of the AFM images suggest that flake thickness varies with flake sizes with thinner flakes being smaller in size.

In order to elucidate the structure of the 2D metal diborides at the atomic scale, we carried out aberration-corrected high resolution TEM (ACTEM) studies of HfB_2. Figure 2.3a shows a multilayer HfB_2 flake composed of 4-5 boron layers. Multiple grains

visible in the TEM image are a consequence of liquid-exfoliation. Ultrasonication shears the sheets apart after which they can restack in different orientation. During the one-hour long sonication, this process may occur thousands of time resulting in nanosheets stacked at different orientations and hence, not showing a uniform hexagonal symmetry throughout the multilayer flake (see Figure A2 in Appendix A for further example). Imaging of the same sample at increased magnification (Figure 2.3b) revealed the hexagonal structure of the hafnium diboride, similar to that of the bulk crystal form. For more detailed comparison with HfB_2, we used density functional theory (DFT) to simulate the TEM image of monolayer HfB_2. We found that the experimental images closely match the simulated structure along the [0001] plane (Figure 2.3b, 2.3c). However, the angles of the hexagon are not precisely the same suggesting distortions in the lattice. A possible reason for this deviation may be that boron sheets are not completely planar, but instead are puckered as found for rectangular borophene[22].

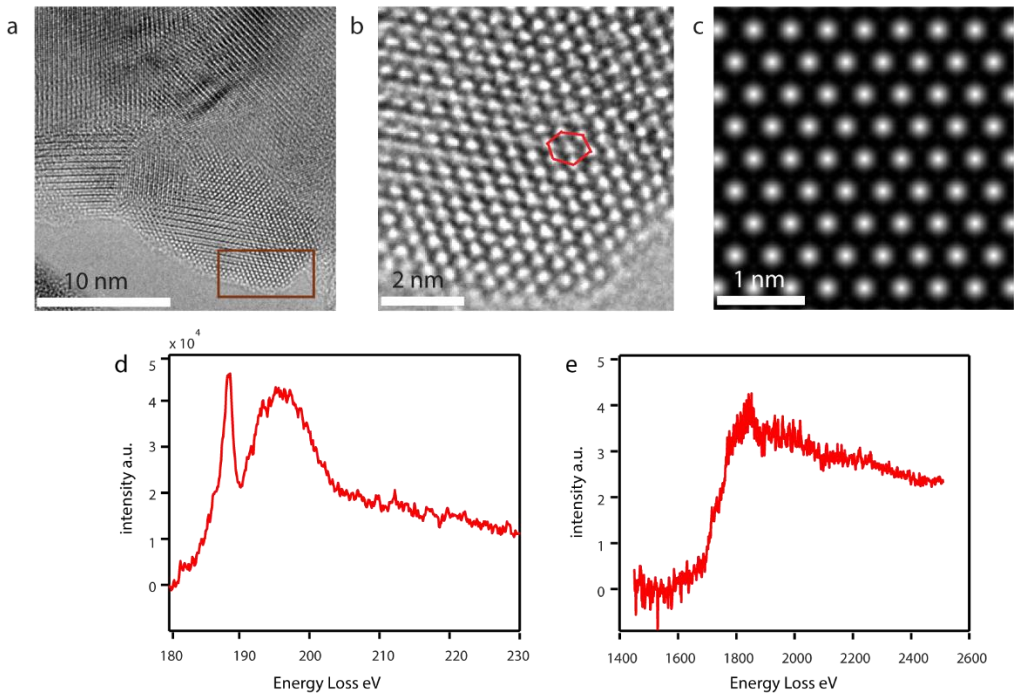

Figure 2.3 | Atomic structure and composition of 2D metal diborides. a, Aberration-corrected TEM image of an HfB_2 nanosheet consisting of 4-5 boron layers. Scale bar is 10 nm. **b**, Zoomed in image of the area indicated in a revealing a hexagonal lattice of atoms in the hafnium diboride. Scale bar is 2 nm. **c**, Simulated TEM image of the HfB_2 bulk crystal structure. Scale bar is 1 nm. **d**, EELS of B, K-edge. **e**, EELS of Hf, M-edge.

2.3.3. Compositional analysis of MB_2

Electron energy loss spectroscopy (EELS) was used to identify the elemental makeup of the metal diborides. The electron energy-loss of the B K-edge in Figure 2.3d shows the characteristic peaks of diboride. The peak at 188 eV corresponds to the transitions to the π^* antibonding state which originates from the sp^2 bonding present within the boron layers and the broad peak centered at 196 eV can be associated with the transitions to the σ^* antibonding orbitals[102]. In figure 2.3e the broad peak above 1800 eV corresponds to the Hf M-edge confirming the presence of hafnium metal[103]. Furthermore, a single EELS spectrum containing both B K-edge and Hf M-edge was collected and used to determine the hafnium to boron ratio of about 34:71, which is approximately equal to the expected value of 1:2 (Figure 2.4). These results show that the chemical composition of pristine HfB_2 is maintained after exfoliation and that HfB_2 does not undergo any chemical change, such as oxidation, due to sonication. These spectra were taken at multiple locations on the nanosheet and little to no spatial variations were found.

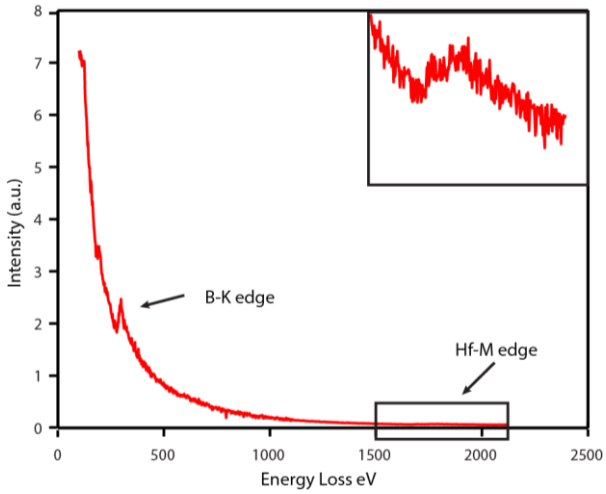

Figure 2.4 | EELS analysis of HfB_2. An EELS spectrum containing both B K-edge and Hf M-edge in a single spectrum and the inset is the zoomed-in image of the boxed part of the spectrum.

MgB_2 nanosheets were also characterized using ACTEM. The EELS spectrum shows two similar peaks for B K-edge as obtained for HfB_2 (Figure 2.5). The peak at 193 eV corresponds to the transitions to the π* state and the broad peak centered at 200 eV represents the transition to the σ* state. The energy dispersive x-ray spectroscopy (EDS) reveals the Kα peak for Mg at 1.25 KeV and also shows a small peak at ~0.5 KeV which correspond to the Kα for oxygen. The peak possibly originates from limited oxidation of MgB_2 during the sonication process.

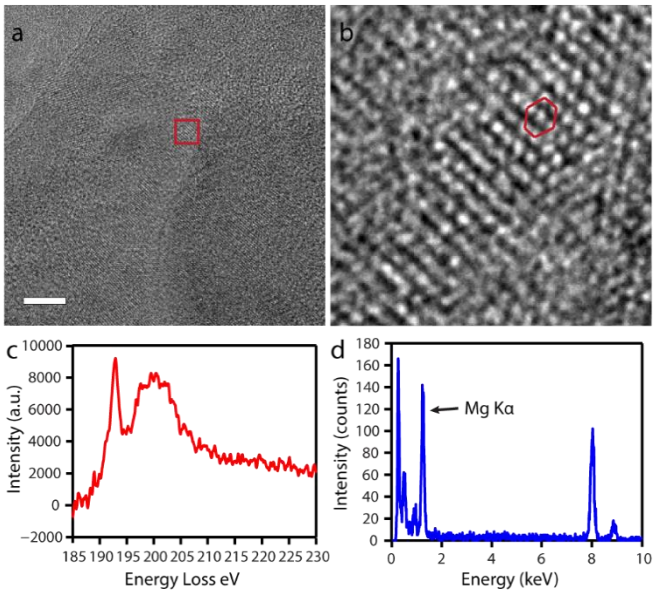

Figure 2.5 | Structural and compositional characterization of magnesium diboride. **a,** is an ACTEM image of MgB_2 with a 5 nm scale bar. **b**, is a zoomed in image of **S2a** showing the hexagonal crystal structure of MgB_2 flake. **c**, is an EELS spectrum showing the B K-edge for MgB_2 and the shape and position of the peaks indicate diboride composition. **d**, is an EDX spectrum obtained for magnesium diboride clearly showing the Mg Ka peak at 1.25 keV.

2.3.4. Synthesis and mechanical testing of PVA-CrB_2 composites

Our metal diboride dispersions enable application of boron sheets in macroscopic forms unavailable to borophenes produced at small scale in UHV conditions[22,79]. They allow metal diboride compounds, which are typically processed at >1000°C temperatures[75,104], to be integrated into low-temperature solution-phase processing methods. As a demonstration of these new scalable sample preparation capabilities for metal diborides, we chose to integrate the exfoliated 2D nanoflakes into macroscopic polymer composites. Theoretical studies have predicted that borophene sheets could provide mechanical stiffness that matches or even exceeds that of graphene[22]; however, the challenges of existing growth methods make direct testing of their mechanical

properties unlikely. After testing several metal diborides, we found that CrB_2 could readily produce stable, high concentration dispersions in 1% aqueous polyvinyl alcohol (PVA) solution following ultrasonication. The CrB_2-PVA dispersions were further diluted with 5% PVA solution and were formed into films by solution casting (see Experimental Methods). The ratio of CrB_2-PVA dispersion and the pure PVA solution was varied to obtain composites with different mass fractions of CrB_2 and the mechanical strength of multiple polymer membranes was measured.

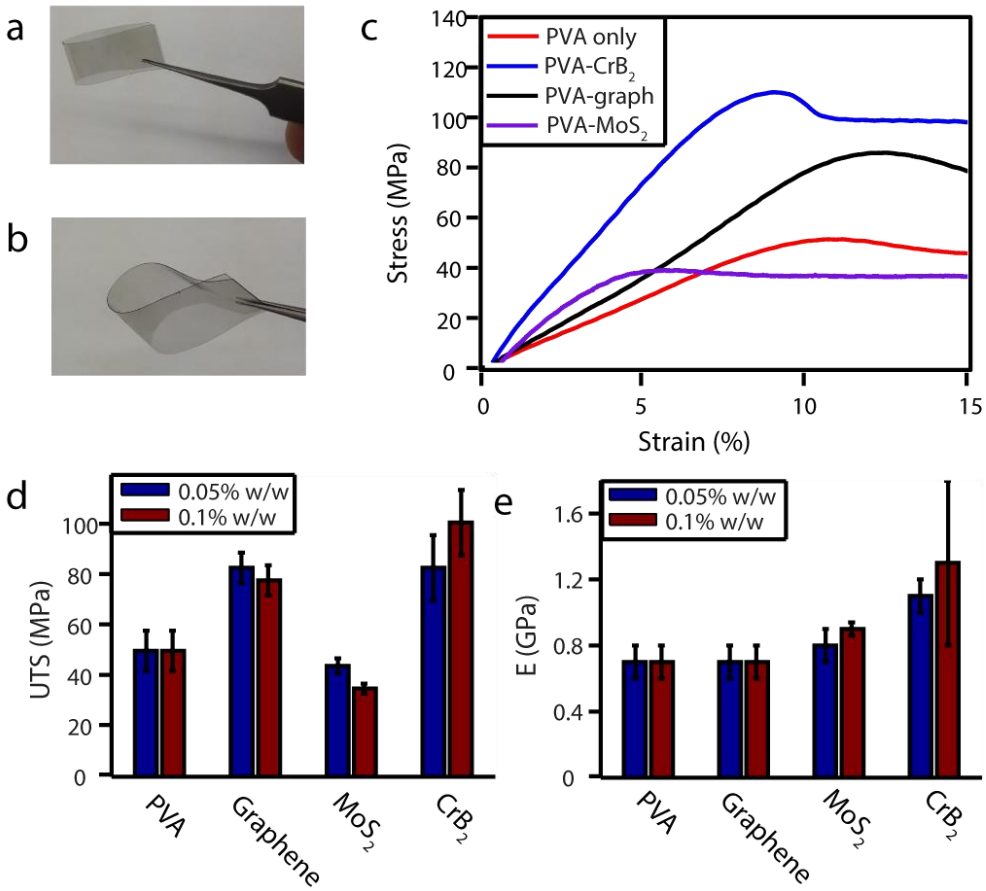

Figure 2.6 | Mechanically reinforced polymer membranes with chromium diboride additives. a-b, Photographs of flexible PVA-CrB_2 composites with a 0.05% (a) and 0.1% (b) mass fraction. **c**, Table showing the average changes in the ultimate tensile strength (UTS), the elastic modulus (E), and the strain at UTS. **d**, Representative stress-strain curves of 0.1% CrB_2-PVA, 0.05% CrB_2-PVA, and PVA-only composites. Both CrB_2-PVA composite films provide substantial increases in elastic modulus and ultimate

tensile strength. **e**, Comparison of percent increases in UTS and E for chromium diboride with other exfoliated 2D materials. Chromium diboride provides increases in strength that are superior to previously well-known materials.

The polymer composites remained quite flexible with the addition of CrB_2 at 0.05% and 0.1% mass/mass loadings (Figure 2.6a and 2.6b). PVA composites of graphene and MoS_2 were also synthesized using the same method for comparison. We found that CrB_2-PVA composites exhibit a 100% increase in the ultimate tensile strength (UTS) and a 94% increase in the Young's modulus (E) with the introduction of 0.1% CrB_2. The strength of the composite increased when the chromium diboride loading was increased from 0.05% to 0.1%; however, the UTS dropped drastically when the concentration was increased to 0.2% and the film also became very brittle. The UTS for graphene-PVA increased by 56% whereas the UTS for MoS_2-PVA decreased by 31%. E for graphene composites was the same as that for PVA on average and increased only by 27% for MoS_2-PVA demonstrating the remarkable reinforcing capability of CrB_2.

2.4. Discussion

The bonding character of metal diborides is different from traditional materials which generally possess weak Van der Waals forces between layers. In the case of metal diborides, the boron atoms serve as electron acceptors and metal atoms behave as electron donors and this donor-acceptor interaction introduces the ionic character in the M-B bond. However, partial interaction of *d*-electrons and the formation of *spd*-hybrid configurations impart covalent character to the M-B bond leading to a complex bonding environment[75]. The ability to exfoliate these compounds using ultrasonic acoustic cavitation demonstrates a major advancement in our ability to prepare two-dimensional

materials from compounds possessing strong interlayer bonding albeit with asymmetrical binding.

Apart from possessing a wide array of properties, metal diborides also share some key characteristics. Most of the metal diborides are brittle, hard, and have high-melting temperatures. Thus, production of metal diboride dispersions represents a significant advance for colloidal processing of ceramic materials. The ability to produce stable, homogeneous and high-concentration dispersions of ZrB_2 and HfB_2, materials that have melting temperatures of 3040°C and 3250°C, respectively, is an enabling step for processing of UHTCs using scalable, low-temperature solution-phase methods.

Direct integration of chromium diboride nanosheets in polymer composites and its superior reinforcement capability compared to as-produced sheets of previously well-known two-dimensional materials such as graphene and MoS_2 makes it an exceptional candidate for structural reinforcement applications. Moreover, chromium diboride nanosheets offer superior structural performance in composites compared to previous work employing two-dimensional materials such as graphene[34], MoS_2[94], and BN[95], and are matched only by graphene after it has been subjected to complex size-sorting procedures. The method we used to produce these composites varies from the traditional approach as we use 1% PVA solution itself as a dispersing agent whereas previously nanosheets were first dispersed in an organic solvent and then used to produce the nanomaterial-PVA composites. This direct approach requires less processing to aid with future efforts at industrial scale-up and promotes stronger interactions between the polymer and nanosheets in the composite.

Given our success at producing eight 2D metal diborides, we anticipate that this method can be generalized to produce two-dimensional diborides from other metal diboride precursors of similar crystal structure, providing a whole new family of 2D materials with a distinct set of properties. Our work can thus pave the way towards the development of hitherto unknown technologies such as spray-on superconductors and UHTCs, nanocomposites of UHTCs, and, given the biocompatibility of constituent atoms such boron and titanium, a unique class of nanomaterials to exploit for biomedical applications. Furthermore, we anticipate that performance of 2D metal diborides can be enhanced by using solution-phase sorting techniques to produce larger and thinner flakes[92], synthesizing modified metal diborides via intercalation methods[25], and developing surface functionalization techniques to modify their properties[105]. Chemical functionalization techniques have the potential to not only tailor the interaction of metal diborides with the environment but may also lead to interesting changes in their optical and electronic properties.

2.5. Conclusion

We have produced a new class of boron-based 2D materials, the metal boridenes, using ultrasonication-assisted exfoliation. We demonstrate the production of bulk quantities of high-concentration dispersions of eight different metal diborides from their respective metal diborides and predict that our method can be generally applied to other structurally similar metal diborides as well. ACTEM and EELS were used to show that the crystal lattice and chemical composition are preserved after exfoliation. To extend the scope of our method, we prepared polymer composites with as-exfoliated chromium

diboride which showed a remarkable increase in the mechanical strength of the composite without resorting to size sorting. We believe our method will open the path towards unconventional applications of 2D materials such as production of spray-on superconductors, nanocomposites of ultra-high temperature ceramics and hybrid 2D materials with a unique set of properties.

2.6. Methods

2.6.1. Materials

All chemicals were used as received without further purifications. MgB_2, AlB_2, TiB_2, NbB_2, TaB_2, polyvinyl alcohol (PVA), sodium cholate (SC), myristyltrimethylammonium bromide (MTAB), N, N-dimethyl formamide (DMF) and 1-methyl-2-pyrollidinone were obtained from Sigma Aldrich. CrB_2 was purchased from Alfa Aesar and ZrB_2 and HfB_2 were obtained from Smart Elements.

2.6.2. Preparation of metal diboride dispersions

0.4 g of the respective metal diboride powder was added to a 15 mL centrifuge tube along with 6 mL of the organic solvent or aqueous surfactant solution (1%). Then the mixture was probe sonicated (Branson Digial Sonifier 450D, 4 mm diameter tip) for 1 hour at an amplitude of 20% corresponding to 11-13 W of power output. The resulting dispersion was transferred into 1.5 mL tubes and centrifuged at 5000 rcf for 4 minutes and top 1 mL of the dispersion was collected from each tube. The concentration of each dispersion was measured by ICP-MS.

2.6.3. Optical absorbance spectroscopy

To collect UV-Vis spectra, the dispersions were diluted as needed and the appropriate solvent or aqueous surfactant solution was used as blank and then UV-Vis-NIR spectra were collected from 400 to 1000 nm in quartz cuvettes.

2.6.4. Transmission electron microscopy

TEM images in Figure 2 and Figure S2 were acquired on Philips CM 12 at 80 kV and aberration corrected HR-TEM images in Figure 3 and S3 were obtained on FEI Titan at 300 kV. Shery Chang performed the DFT simulations using in-house program based on Multislice method modified from Kirkland's method[106] to generate the simulated HfB_2 TEM image. The simulated parameters correspond to the experimental TEM conditions, with accelerating voltage of 300kV, spherical aberration of -14μm (which corresponds to the optimum phase contrast imaging condition of negative Cs imaging), and defocus of 10 nm.

2.6.5. EDX and EELS

EDX spectra were also collected on the Titan as well, however, EELS was performed on ARM 200F equipped with an Enfinium EELS spectrometer operated at 300 kV. EDX and EELS spectra were collected with Shery Chang's assistance.

2.6.6. Atomic force microscopy

AFM imaging was carried out on a Multimode V system (Bruker Corp.) with ScanAsyst-Air tips (Bruker) in ScanAsyst noncontact mode. Gwyddion was used for image processing. Dispersions of HfB_2 were prepared in isopropanol using the procedure as mentioned above. A drop of the above dispersion was spin coated onto a pre-exfoliated

HOPG substrate at 3000 rpm for 1 min. Spin coating was repeated five times to increase the yield of deposited nanosheets. AFM was done by Ximo S. Chu.

2.6.7. Polymer composite preparation and tensile measurement

To synthesize composites with PVA, 1.3 g of chromium diboride was sonicated in 20 mL of 1% aqueous PVA solution for 1 hour at 30% amplitude and the resulting suspension was distributed equally in 1.5 mL tubes and centrifuged at 5000 rcf for 5 minutes. The concentration of the resulting dispersion was determined by ICP-MS and it was used to calculate the mass loading of the CrB_2 in the composites. The above dispersion was mixed with 5% aqueous PVA by vortexing to obtain the required concentrations and then it was bath sonicated for 20 minutes. A 24-mL volume of the above dispersion was poured in a Petri dish and dried in an oven at 60°C for 48 hours. The resulting membranes were peeled from the Petri dishes, cut into rectangular pieces (3 cm x 1 cm) and their thicknesses were measured. Then these were tested mechanically using a MTII/Fullam SEM tester (MTI Instruments Inc.) at a strain rate of 0.05 mm/s. At least three strips were measured for each nanosheet concentration. Fraaz Tahir assisted with the measurements.

Chapter 3

Understanding Dispersibility of Metal Diborides in Organic Solvents

3.1. Introduction

Metal diborides (MB_2) are a new class of boron-rich two-dimensional materials that are derived from bulk metal diborides through ultrasonication. The structure of metal diborides consists of stacks of hexagonal sheets of boron, similar to graphene, with metal atoms sandwiched between them. Metal diborides with different metal atoms in between the boron layers exhibit a wide set of properties. For instance, magnesium diboride is a well-known superconductor[73] with a transition temperature of 39 K. Aluminum diboride is known to possess metallic conductivity.[107] Titanium diboride is a ceramic that exhibits electrical conductivity higher than titanium itself.[108] Hafnium and zirconium diborides are ultra-high temperature ceramics[75] with potential applications in atmospheric reentry vehicles.

Understanding the dispersion behavior of the 2D metal diborides in diverse solvents is important as it can help us predict the ideal solvent for exploiting these nanosheets in different applications and also shed light on the mechanisms of interaction between solvent molecules and the nanosheets. In basic solubility theory, cohesive energy density is central to defining the solubility of molecular solutes.[109] Cohesive energy density, $E_{C,T}/V$, where $E_{C,T}$ is the total molar cohesive energy and V is the molar volume of solvent, can be further divided into three components: dispersive $E_{C,D}/V$, polar $E_{C,P}/V$, and hydrogen-bonding $E_{C,H}/V$, and can be written as follows:

$$\frac{E_{C,T}}{V} = \frac{E_{C,D}}{V} + \frac{E_{C,P}}{V} + \frac{E_{C,H}}{V}$$

To define solubility, the Hildebrand solubility parameter, δT, is most commonly used. δT is calculated by taking the square root of cohesive energy density and the Hansen solubility parameters, δD, δP, and δH, are the square roots of each of the three components of cohesive energy density.

$$\delta_T^2 = \delta_D^2 + \delta_P^2 + \delta_H^2$$

The entire theory is based on the principle of *like dissolves like*. For nonpolar solutes, Hildebrand parameter, for both, solvent and solute should be very close, whereas for polar solutes, similar values of all the Hansen parameters for solute and solvent are also generally required[110]. For graphene and TMDCs[45,46], it has been shown that their dispersibility in a solvent can be predicted by comparing their Hildebrand and Hansen solubility parameters (THSP). Previous work by the Coleman group has demonstrated that the closer the THSP of a solvent is to that of the nanomaterial, the higher is the dispersibility[45,46] (*like dissolves like*). In order to study the effect of solvents on dispersion behavior of the metal diborides, we carried out a detailed study using AlB_2, TiB_2 and HfB_2 as our model materials. For this purpose, we screened 33 different solvents against the three metal diborides and determined their HSP. Furthermore, we also show how the dispersibility of the three materials varies with surface energy of the solvent.

3.2. Results and discussion

To prepare the MB_2 dispersions, 0.4 g of the bulk metal diboride powder was sonciated using a proble sonicator in 6 ml of the respective solvent for one hour at 20% power (12-13 W) and the resulting dispersion was centrifuged at 5000 rcf for 4 minutes. UV-Visible

spectroscopy was used to obtain the absorbance from each dispersion. The absorbance obtained is directly related to the concentration of the material and was used as a measure of the dispersibility of MB_2. The HSP for the solvents were obtained from literature[45] and the ones for AlB_2, TiB_2 and HfB_2 were estimated by taking weighted average of the HSP of the solvents.

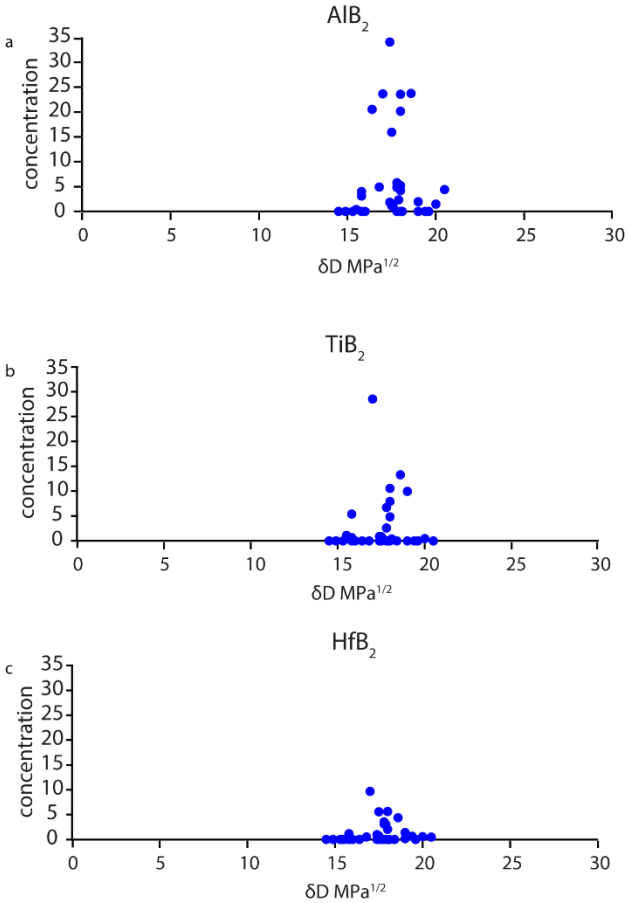

Figure 3.1 | Dispersibility of metal diborides as a function of Hansen Solubility Parameter δD. Dispersibility of AlB_2, TiB_2, and HfB_2 in 33 different solvents tested as a function of dispersive (δD) Hansen solubility parameters

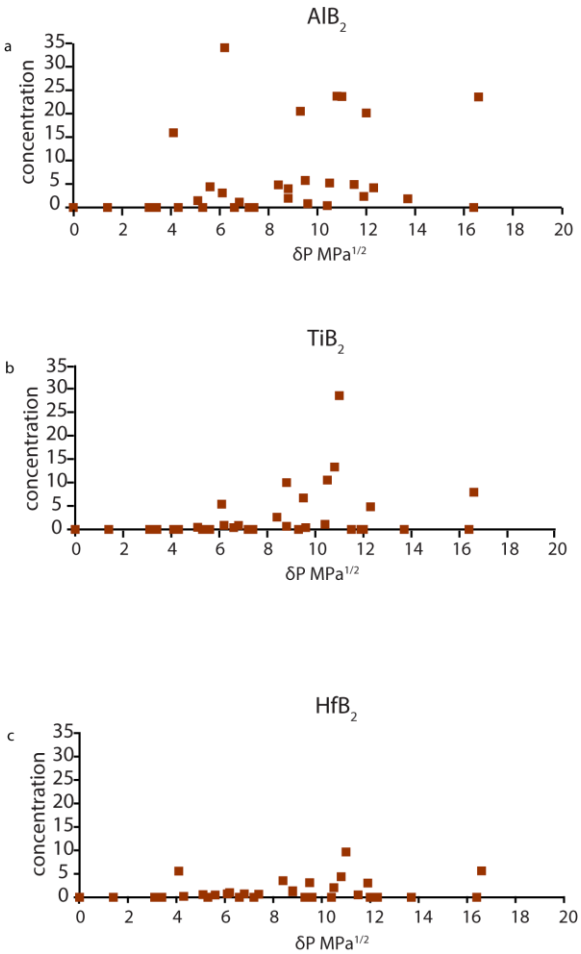

Figure 3.2 | Dispersibility of metal diborides as a function of Hansen Solubility Parameter δP. Dispersibility of AlB_2, TiB_2, and HfB_2 in 33 different solvents tested as a function of polar (δP) Hansen solubility parameters

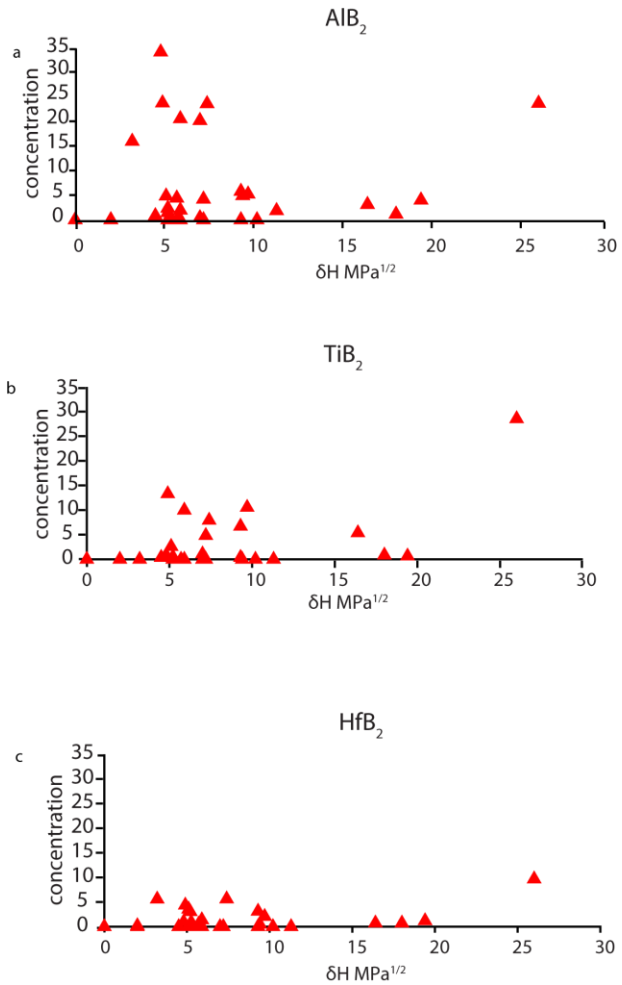

Figure 3.3 | Dispersibility of metal diborides as a function of Hansen Solubility Parameter δH. Dispersibility of AlB_2, TiB_2, and HfB_2 in 33 different solvents tested as a function of hydrogen bonding (δH) Hansen solubility parameters

Figure 3.1-Figure3.3 shows the dispersibility of AlB_2, TiB_2 and HfB_2 as a function of the the Hansen solubility parameters where each point refers to a dispersion of the respective MB_2 in the solvent with respective Hansen parameter value. From these plots, the Hansen solubility parameter values can be estimated using the following equation:

$$< \delta_i > = \frac{\sum_{solvent} C_{MB} \delta_i}{\sum_{solvent} C_{MB}}$$

Here δ referes to the solubility parameter of the MB_2, i is T,D,P, or H, and C_{MB} is the concentration of MB_2 in the respective solvent. The calculated values are shown in Table

1. These results show that the value of dispersive (δD) and the polar (δP) Hansen parameters are almost the same for all three diborides at ~17.6 $MPa^{1/2}$ and ~10 $MPa^{1/2}$, respectively. However, the δH is appreciably different. The table also shows a comparison of these values with graphene[45] and MoS_2[46] that were previously reported. These numbers are similar to the ones reported for other two-dimensional materials, except for the δH which varies with the diboride.

We also calculated the Hildebrand solubility parameter, δT, using similar methods and found it to be 20.7 $MPa^{1/2}$ for AlB_2, 23.0 $MPa^{1/2}$ for TiB_2 and 22.5 $MPa^{1/2}$ for HfB_2. Figure 3.2 shows the dispersibility as a function of the Hildebrand parameter.

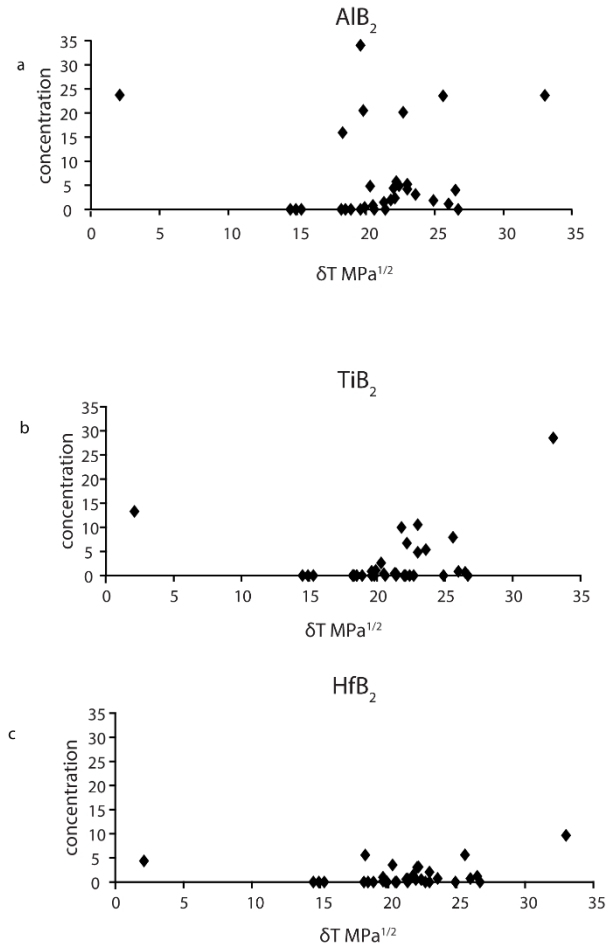

Figure 3.2 | Dispersibility of metal diborides as function of Hildebrand Parameter. Dispersibility of AlB_2, TiB_2, and HfB_2 tested as a function of Hildebrand (δT) solubility parameter in 33 different solvents

The solvents that give the highest dispersibility are N-octylpyrollidinone (δD =17.4, δP = 6.4, δH = 4.8, δT = 19.6) for AlB_2, and ethylene glycol (δD = 17, δP = 11, δH = 26, δT = 33) for TiB_2 and HfB_2. However, we note that ethylene glycol is a very viscous solvent and the centrifugation under similar conditions might not be suitable enough to remove all of the unexfoliated MB_2. In case of TiB_2 and HfB_2 the next best solvents are dimethylphthalate (δD = 18.6, δP = 10.8, δH = 4.9, δT = 22.1) and 1-dodecyl-2-pyrollidinone (δD = 17.5, δP = 4.1,δH = 3.2, δT = 18.3) respectively. We also note that

solvents with near zero polarity (pentane, hexane, heptane, and toluene) show no dispersibility.

Materials	**<δD>** **$MPa^{1/2}$**	**<δP>** **$MPa^{1/2}$**	**<δH>** **$MPa^{1/2}$**	**<δT>** **$MPa^{1/2}$**
AlB_2	17.6	9.9	**8.8**	20.7
TiB_2	17.7	10.6	**13.5**	23.0
HfB_2	17.7	10.0	**11.0**	22.5
Graphene[45]	18	9.3	**7.7**	23
MoS_2[46]	17.8	9	**7.5**	22

Table 3.1 | Solubility parameters of metal diborides. All values are similar to those for graphene and MoS_2 except for the δH, which are emphasized in bold

Figure 3.3 shows the TEM images of the dispersions in the best solvents for AlB_2 and HfB_2 and the second best solvent for TiB_2, dimethylphthalate (DMP). These images confirm the two-dimensional nature of the nanosheets and show flakes in the size range of a 50 nm to 1 μm with flat or folded morphology. It is evident from TEM analysis that TiB_2 and HfB_2 dispersions in ethylene glycol contain some thicker alongwith the thinner, two-dimensional flakes as well.

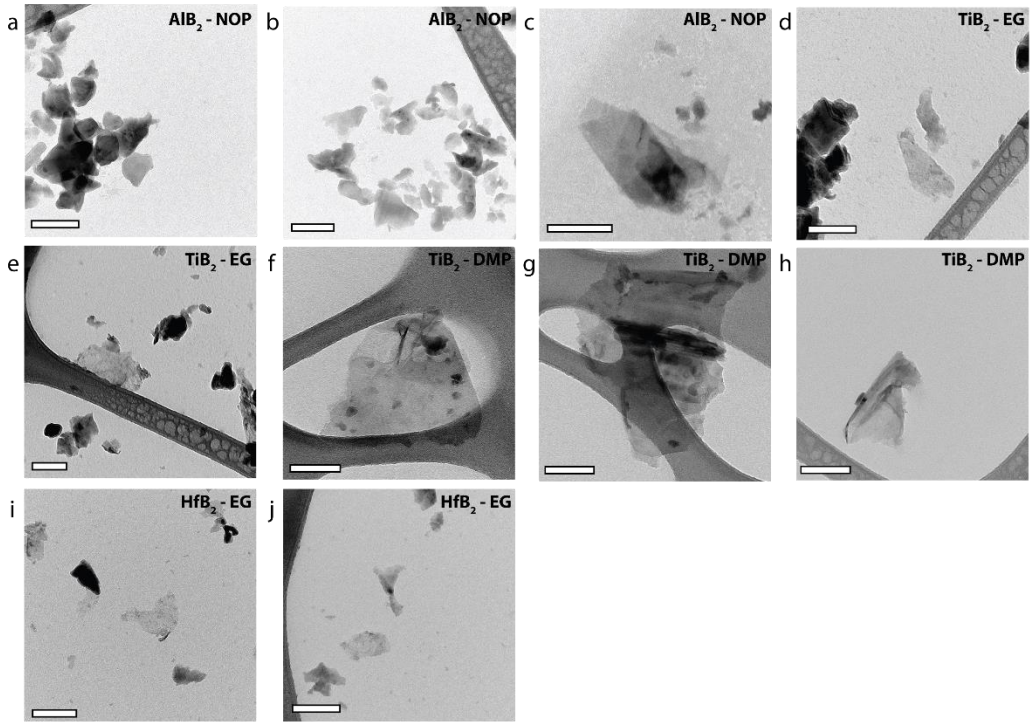

Figure 3.3 | TEM images of metal diborides in selected solvents. TEM images of **a-c**, AlB_2 in 1-octyl-2-pyrollidinone (NOP) **d-e**, TiB_2 in ethylene glycol (EG) **f-h,** TiB_2 in dimethyl phthalate (DMP) and **i-j**, HfB_2 in ethylene glycol confirming two-dimensional nature of the nanosheets. Scale bar in all images is 100 nm.

Exfoliation in organic solvents is only possible if the overall energy cost for the process is low. Hernandez et al. developed a model for exfoliation of graphene where the balance between surface energies of solvent and graphene describe the enthalpy of mixing[91]. The equation they developed is given below:

$$\frac{\Delta H_{mix}}{V_{mix}} \approx \frac{2}{T_{flake}} (\delta_G - \delta_{sol}) 2\varphi$$

where $\Delta H_{mix}/V_{mix}$ is the enthalpy of mixing per unit volume, T_{flake} is the thickness of flake, δi is the square root of surface energy of i, and φ is the volume fraction of graphene. From this equation, we can see that the energy cost of exfoliation will be minimum when the surface energy of the solvent and graphene is similar. The same model can be

generally applied to all two-dimensional materials including the metal diborides. Figure 4 shows the relationship between surface tension of the solvents, which is a direct measure of their surface energy, and the concentration of dispersions of AlB_2, TiB_2, and HfB_2. We can observe from the plots that most of the efficient solvents lie at surface tension values above 30 dynes/cm. If we take a weighted average from the data, we get an average value of surface tension as 39.8 dynes/cm, 41.8 dynes/cm, and 40.2 dynes/cm for AlB_2, TiB_2, and HfB_2 respectively. This is in good agreement with the surface tension values for graphene and TMDCs reported in literature.

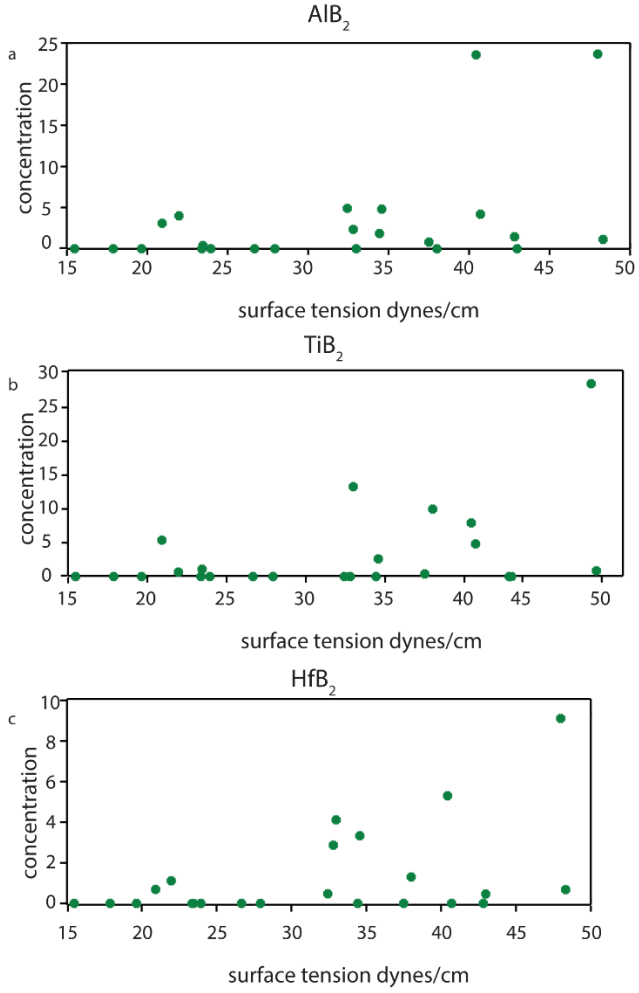

Figure 3.4 | Dispersibility of metal diborides as a function of surface tension.

3.3. Conclusion

In conclusion, we demonstrate how the dispersibility of three metal diborides, AlB_2, TiB_2, and HfB_2, in organic solvents vary with Hansen solubility parameters, Hildebrand parameter, and surface energy. Although most of these parameters are similar to those determined previously for graphene and TMDCs, δH for the metal diborides is very different for all three diborides and differs substantially from those of graphene and MoS_2. These results give useful insight into the process of exfoliation and may be used to calculate the energy cost of exfoliation. Furthermore, solvents best suited for dispersing metal diborides are also identified and can be used for various applications such as making composites of metal diborides with polymers.

3.4 Experimental Section

To prepare metal diboride dispersions, 0.4 g of AlB_2, TiB_2, and HfB_2 were measured into a 15 ml centrifuge tube and 6 ml of respective solvent was added. The resulting mixture was probe sonicated (Branson Digital Sonifier 450D, 4 mm tip) for 1 hour at 20% amplitude. The resulting dispersions were transferred to 1.5 ml tubes and centrifuged at 5000 rcf for 4 mins and top two-third of the supernatant was collected and their absorbance spectra recorded using Jasco UV-Vis-NIR Spectrophotometer 670 in quartz cuvettes. TEM imaging was carried out on a Philips CM 12 at 80 kV by drop-casting samples on holey 400 mesh Cu grids (Ted Pella Inc.) with ultrathin carbon layer. Matthew S. Gilliam prepared a few of these dispersions using the same protocol.

Covalent Functionalization of Pristine Two-Dimensional Molybdenum Disulfide and Attachment of Functional Proteins

4.1. Introduction

Two-dimensional transition metal dichalcogenides (TMDCs) are a class of structurally related materials with remarkable electronic, optical, and chemical properties.[25] In the past few years, these materials have been explored for a wide range of applications including electronics,[50,52,53,96] optoelectronics,[26,58,61,111,112] and catalysis[113] (see section 1.3.1). Their nanoscale dimensions, large surface-to-volume ratio, and intrinsic photoluminescence also make them promising candidates for various biological applications such as drug and gene delivery (see section 1.3.2).[63,67–69] We can further expand the scope of these materials by engineering their surface properties to control their interactions with their environment. For low dimensional materials, chemical modification of their surfaces can also lead to changes in their chemical, optical and electronic properties.[114–117] Doping,[118] functional group interconversion[114] and tethering of small molecules[119–121] and polymers[122] are some of the strategies that have been used for this purpose.

Surface modification of MoS_2, the archetypal TMDC, has been previously established using a variety of different techniques. Many of these methods utilize non-covalent functionalization methods involving physisorption of organic or inorganic moieties on the surface, but they are less robust.[123–125] Several covalent functionalization approaches to MoS_2 functionalization have been reported as well. However, they either utilize harsh treatments such as the use of $TiCl_4$[126] or involve reaction at defect sites limiting the degree of functionalization to initial defect concentration.[124] For liquid-exfoliated MoS_2, covalent modifications have been shown only after lithium intercalation of MoS_2 with alkyl lithium compounds.[127] These methods are limited not only by the use of pyrophoric alkyl lithium compounds but also by the phase change of MoS_2 from the 2H-phase to the 1T-phase that accompanies the lithiation process. As a result, MoS_2 goes from semiconducting to an electron-rich metallic phase with different chemical properties. However, there are no methods reported that provide a route to direct covalent functionalization of pristine, unmodified MoS_2 without using harsh treatments.

To overcome this problem, we carried out covalent functionalization of MoS_2 by directly reacting it with aryl diazonium salts under mild conditions. The method is robust, does not require any pretreatment, and can be applied to MoS_2 produced using a variety of synthetic approaches including mechanical exfoliation, CVD, and liquid-phase exfoliation. Most of the work on mechanically exfoliated and CVD-grown MoS_2 was carried out by Ximo S. Chu and Duo O. Li and can be accessed through the paper cited at the beginning of the chapter. This chapter will discuss the work done with liquid-

exfoliated MoS_2 and protein attachment experiments on the mechanically exfoliated MoS_2.

The dispersion and subsequent diazonium functionalization of pristine, liquid-dispersed MoS_2 was carried out by an ultrasonication-mediated process, eliminating the need for harsh lithium treatment. Covalent attachment of the aryl group on MoS_2 surface was confirmed by Fourier transform infrared spectroscopy (FTIR) and thermogravimetric analysis (TGA). An excitonic peak in the optical absorbance spectrum of the functionalized MoS_2 showed a red shift after reaction with aryl diazonium salts. Furthermore, we demonstrate the utility of the technique by grafting the fluorescent proteins GFP and mCherry to the surface of mechanically exfoliated MoS_2 and confirm their activity by confocal microscopy. A 1:1 mixture of GFP and m-Cherry was also uniformly attached on the surface of MoS_2 to demonstrate the robustness and flexibility of the process. The direct covalent modification of the MoS_2 surface suggests many future opportunities to enhance the properties of TMDCs via mild chemistries and provides a versatile chemical platform for tailoring the properties of MoS_2 simply by functionalizing with different aryl diazonium salts.

4.2. Experimental Section

4.2.1. MoS_2 dispersions and functionalization in solution

MoS_2 was dispersed in sodium dodecyl sulfate (SDS) aqueous solution by microtip probe sonicating (Branson Digital Sonifier 450D, 13 mm diameter tip) 8.25 g of MoS_2 in 110 mL of 1% SDS solution (w/v) for 2 hours in a 250 mL steel beaker at 50% amplitude (power output of 48-50 W). Then 25 mL of this dispersion was transferred in 4

separate 50 mL plastic tubes and centrifuged at 4200 rpm for 3.5 hours to remove large, undispersed particles. To carry out the functionalization, 100 mg of the diazonium salt was added to 20 mL of the MoS_2-SDS dispersion and probe sonicated for 2 hours at 20% amplitude with a 3 mm diameter tip in a 50 mL tube. The resulting functionalized dispersion was flocculated with ethanol and filtered over a hydrophilic PTFE membrane (Omnipore, 100 nm pore size) and washed thoroughly with water and ethanol, resulting in a dry film collected on the membrane.

4.2.2. FTIR and UV-vis characterization of bulk dispersions of MoS_2

The dried films of functionalized MoS_2 on filter membrane were used to collect Fourier transform infrared (FTIR) spectra using a Nicolet 6700 system equipped with a Smart Orbit accessory. To re-suspend the samples in solution, the filter membranes were placed in 50 mL tubes along with 15 mL of SDS solution and bath sonicated for 2 hours. After sonication, the dispersions were filtered using Millipore vacuum filtration system (20 μm pore size) and then their UV-Vis absorbance spectra were collected (Jasco V760 UV-Visible/NIR Spectrophotometer). A control sample was also prepared in parallel using the same conditions as described above, except without the diazonium salt.

4.2.3. Thermogravimetric analysis (TGA) of MoS_2 dispersions

To prepare samples for TGA, 10 mL of the MoS_2 dispersion after 4-NBD functionalization was mixed with acetone in a ratio of 1:5 to aggregate and remove the SDS surfactant. After aggregation, the resulting dispersion was centrifuged for 30 minutes at 5000 rpm. The supernatant was decanted, and the mixture was washed with 40 mL of DI water. The washing step was repeated three times. After washing, the sample

was freeze dried to obtain a solid green powder, which was then analyzed using TGA. A control sample of the SDS-dispersed MoS_2 (without diazonium functionalization) was similarly processed to obtain solid green powder for TGA analysis. TGA samples were prepared by Abhishek Debnath.

TGA characterization was performed using a Setaram TG92 system. Each sample was purged with ultrahigh purity He gas overnight before TGA measurement. The He gas flow rate during the purge and the measurement was 30 mL per minute. The heating ramp rate was 5°C per minute up to 900°C. The first derivative curve (DTG) was calculated in Matlab by first smoothing the TG curve using a Savitzky-Golay filter and then taking the numerical derivative.

4.2.4. 4-carboxybenzenediazonim tetrafluoroborate synthesis and characterization

4-carboxybenzenediazonium tetrafluoroborate (4-CBD) was synthesized following a reported procedure.[128] Briefly, 1.35 g (0.01 mol) of p-aminobenzoic acid was dissolved in 14 ml of water and 3 ml of concentrated HCl. The mixture was cooled in an ice water bath until precipitates appeared. The precipitates disappeared after slow addition of sodium nitrite solution. The sodium nitrite solution was prepared by dissolving 0.752 g (0.011 mol) of sodium nitrite in 4 ml of water. The solution was vacuum filtered and then 1.465 g (0.013 mol) of sodium tetrafluoroborate was added. Then the solution was cooled below 0°C to obtain white crystals, which were then vacuum filtered and washed with ice-cold ether and water. The diazonium salt was dried and then stored at 4°C.

4.2.5. Mechanical exfoliation of MoS_2

SiO_2 (300 nm)/Si substrates (Wafernet, Inc.) were ultrasonically cleaned in sequential baths of acetone and isopropanol and then blown dry with ultrahigh purity nitrogen gas. MoS_2 flakes were prepared on the cleaned substrate by mechanical exfoliation from a bulk MoS_2 crystal (SPI Supplies) using adhesive tape. The samples were then annealed in vacuum at 300°C to remove tape residue and characterize by optical microscopy and atomic force microscopy. The mechanically exfoliated MoS_2 samples were prepared by Ximo S. Chu and Duo O. Li.

4.2.6. Protein synthesis and purification

The green fluorescent protein (GFP) expression plasmid was constructed following previously described methods using the GFP variant GFPmut3b.[129] The GFP gene was inserted into the pET15b (EMD Millipore) expression vector downstream of a T7 promoter and the polyhistidine tag sequence, yielding an N-terminal his-tagged GFP; and upstream of the T7 transcriptional terminator. The resulting plasmid was transformed into *E. coli* BL21 Star DE3. The transformed cells were cultured in 1 ml of LB medium with ampicillin (100 μg/ml) shaking at 37°C in an incubator overnight. The overnight culture was diluted 1:600 with fresh LB medium containing ampicillin (50 μg/ml) and grown until its absorbance at 600 nm reached 0.6-0.8. IPTG (isopropyl β-D-1-thiogalactopyranoside) was added into the culture to a final concentration of 0.5 mM to induce expression of T7 RNA polymerase and in turn trigger GFP production. After 4 hours of induction, the cells were harvested by centrifugation at 4000 *g* for 15 minutes. The cell pellet was resuspended in 27 ml lysis buffer (60 μg/ml lysozyme, 3.7 mM

NaH_2PO_4, 16.3 mM Na_2HPO_4, 50 mM NaCl, 10 mM imidazole, 0.1 Protease Inhibitor Cocktail Tablet/ml) and sonicated at 4 W using a microtip probe (Branson Digital Sonifier 450D, 3 mm diameter tip). Three hundred 2-second pulses with a 2-second off time between each pulse were performed in an ice bath. The lysate was then centrifuged at 12,000 *g* for 30 min at 4°C. Approximately 25 ml of supernatant was collected and filtered through a 0.22-μm membrane filter. Purification was performed using fast protein liquid chromatography (FPLC) with a HisTrap HP column. After equilibrating the column using 100% of Buffer A (3.7 mM NaH_2PO_4, 16.3 mM Na_2HPO_4, 500 mM NaCl, 20 mM imidazole, 0.3 mM TCEP, pH 7.5), 10 mL cleared lysate was loaded into the column, washed with 10% of Buffer B (3.7 mM NaH_2PO_4, 16.3 mM Na_2HPO_4, 350mM NaCl, 500 mM imidazole, 0.3 mM TCEP, pH 7.5) and 90% of Buffer A, and eluted with 50% of Buffer B and Buffer A. Fractions were collected by monitoring the absorbance at 280 nm for the peak in its profile associated with the purified protein. Purified fractions collected from three FPLC runs were concentrated using Amicon (10 kD cutoff filters) and then stored in 50 mM NaH_2PO_4, 300 mM NaCl, pH 8.3. For smaller protein preparations, Ni-NTA spin columns (Qiagen) were used for purifying the His-tagged proteins. mCherry plasmid and protein preparation were performed using the same procedures as those used for GFP. All protein synthesis and purification experiments were performed by Anli A. Tang.

4.2.7. Protein attachment

The protocols used for protein attachment were similar to previous reports of protein attachment to graphene.[105,130] MoS_2 flakes exfoliated onto SiO_2/Si wafers were

immersed in a 10 mM solution of 4-CBD and heated to 53-55°C for 2 hours. Then the samples were washed with water, acetone, IPA and water again sequentially. After drying, they were immersed in a solution of 2 mM EDC and 5 mM sulfo-NHS solution prepared in 2-(N-morpholino)ethanesulfonic acid (MES) buffer (0.1 M MES sodium salt, 0.5 M NaCl, pH adjusted to 6 with 1.0 N HCl) for 20 min. The samples were rinsed with water and immediately immersed into 11.3 mM solution of N_α,N_α-Bis(carboxymethyl)-L-lysine hydrate (NTA-NH_2) prepared in 1x PBS for 2 hr. The wafers were washed with water and dipped in 11.3 mM solution of $NiCl_2$ for 40 min. The wafers were again rinsed with water and immersed in 8 μM solutions of His-tagged GFP or His-tagged mCherry or 1:1 mixtures of the two proteins for 1 hour and rinsed with water twice and then air dried.

4.2.8. Atomic force microscopy imaging

MoS_2 samples before and after protein attachment were characterized using AFM. AFM imaging was conducted using a Multimode V system (Bruker Corp.) with ScanAsyst-Air tips (Bruker) in ScanAsyst noncontact mode. Images were processed using the Gwyddion software package.[131] All AFM experiments were performed by Ximo S. Chu and Duo O. Li.

4.2.9. Confocal microscopy imaging

Confocal fluorescence microscope images were collected with a Leica TCS SP5 Spectral Confocal System using lasers with 488 nm and 561 nm wavelengths.

4.3. Results and discussion

4.3.1 Liquid-phase dispersion and functionalization of MoS_2

Aryl diazonium salts were used to functionalize MoS_2. These reagents have been previously used to covalently functionalize carbon nanotubes,[132,133] graphene,[105,119,134–137] and phosphorene[120], however, these other materials have very different electronic structures and chemical reactivity than MoS_2, which has a highly inert surface. Unexpectedly, we found direct evidence of covalent functionalization of unmodified MoS_2 by aryl diazonium salts. We first used 4-nitrobenzenediazonium (4-NBD) tetrafluoroborate salt in aqueous solution to functionalize MoS_2 (see Experimental section for more details). The reaction shown in Figure 4.1 is expected to proceed through a nitrophenyl radical with the release of nitrogen gas due to charge rearrangement at the surface of MoS_2. This nitrophenyl group attaches on the surface of MoS_2 by forming a S-C covalent bond.

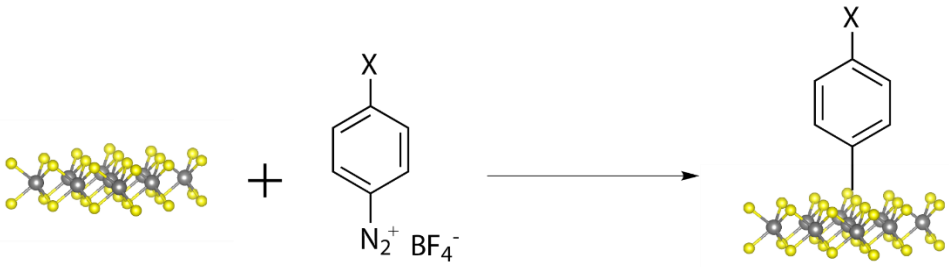

Figure 4.1| Schematic of the MoS_2-diazonium reaction. X can be varied to modify functionality of the molecule. We have shown diazonium chemistry with NO_2 and COOH groups.

The process of dispersion and functionalization is illustrated in Figure 4.2a. Bulk powder MoS_2 was probe-sonicated in an aqueous solution of sodium dodecyl sulfate (SDS) to exfoliate it into sheets that are stabilized by the SDS molecules (Figure 4.2b(i)). Then, 4-NBD was added, and the mixture was probe-sonicated to allow the diazonium

salt and pristine MoS_2 sheets to react. Sonication helped in producing more accessible sites between layers for the diazonium salt to react, encouraging more efficient functionalization. To remove excess 4-NBD, the resulting dispersion was flocculated with ethanol, collected on a filter membrane and washed thoroughly with water and ethanol. (See Experimental section for additional details.) A control sample of unfunctionalized MoS_2 was also prepared following the same procedure but leaving out the 4-NBD functionalization step. The unfunctionalized MoS_2 and functionalized 4-NBD/MoS_2 materials collected on the filter membranes form a continuous thick film with similar colors as their dispersions.

The 4-NBD/MoS_2 and MoS_2 materials collected on the filter membranes were characterized by Fourier transform infrared (FTIR) spectroscopy. In Figure 4.2c, the FTIR spectrum of diazonium-functionalized MoS_2 clearly shows the presence of characteristic peaks that confirmed successful covalent modification MoS_2 in bulk dispersions. The peaks at ~1518 cm^{-1} and ~1344 cm^{-1} represent the stretching vibrations of the N-O bond in the NO_2 group, the peak at 1595 cm^{-1} represents C=C stretching vibrations in the aromatic ring, and the peak at 697 cm^{-1} can be assigned to S-C stretching vibrations at the covalent bond between the MoS_2 surface.

After acquiring the FTIR spectra, the films were re-dispersed in a fresh SDS solution using bath sonication (see Experimental section for further details). The diazonium-functionalized MoS_2 material gave a highly concentrated dispersion after bath sonication (Figure 4.2b(iii)) in contrast to unfunctionalized MoS_2, which was only weakly re-dispersed (Figure 4.2b(ii)). This change in dispersibility can be attributed to a

change in surface energy, a phenomenon which has been previously reported for dispersions of TMDCs,[46,138] and for covalently functionalized graphene.[117,139]

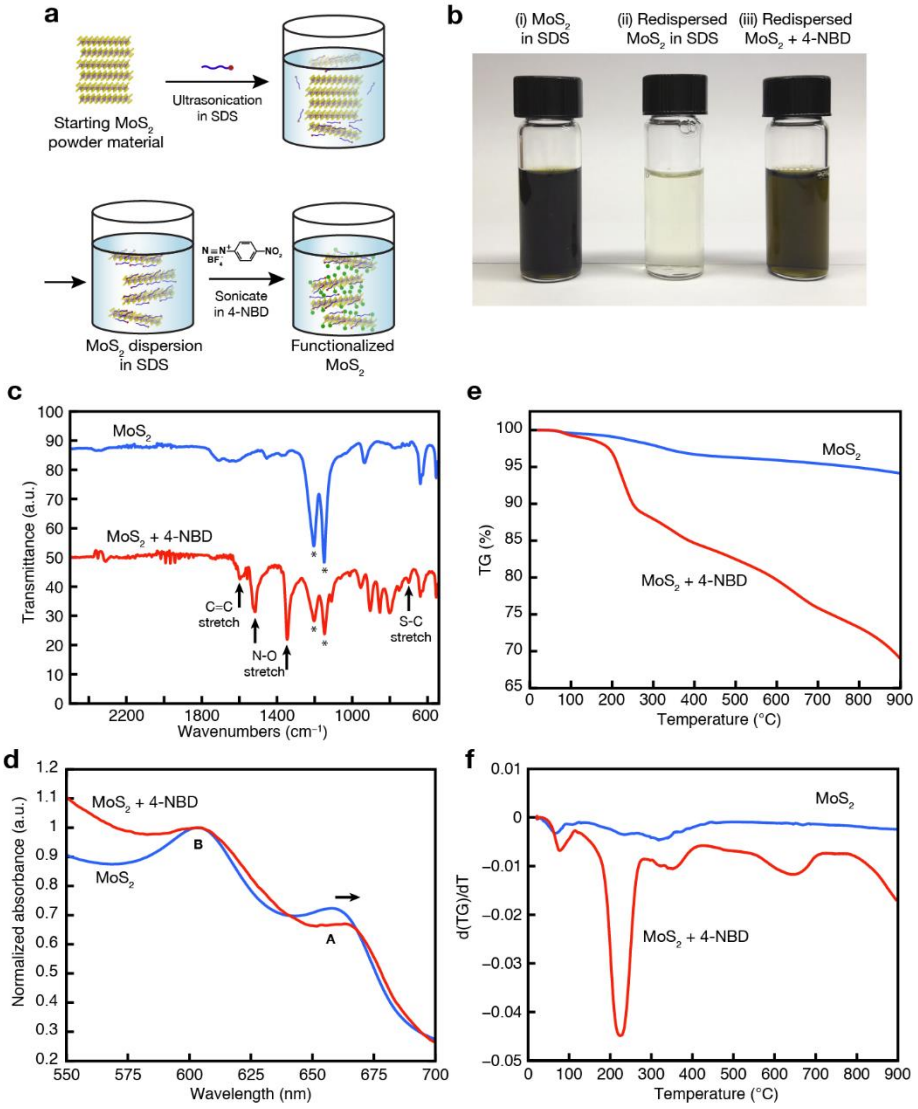

Figure 4.2| Bulk solution phase functionalization of MoS_2. a, Schematic diagram of solution phase exfoliation and functionalization processes. The initial MoS_2 powder material was exfoliated and dispersed by ultrasonication in an aqueous solution of sodium dodecyl sulfate (SDS), which causes thin flakes of MoS_2 to separate and become encapsulated by SDS molecules. The dispersed MoS_2 flakes were then directly functionalized by 4-NBD in solution, resulting in a stable dispersion of covalently functionalized MoS_2. **b**, Photographs of different MoS_2 preparations: (i) a dark green suspension of MoS_2 in SDS; (ii) a pale green suspension of MoS_2 that has been dispersed, dried and restacked, and redispersed in SDS, showing ineffective redispersion after

restacking; and (iii) a dark green suspension of MoS_2 that has been dispersed and functionalized in 4-NBD, dried and restacked, and redispersed, showing that the functionalization allows for effective redispersion. All suspensions were centrifuged to remove undispersed parts. **c**, Fourier transform infrared (FTIR) spectra for dried films of unfunctionalized MoS_2 (blue curve) and 4-NBD functionalized MoS_2 (red curve). Peaks corresponding to the nitrophenyl groups (C=C stretch, N-O stretch) and the covalent functionalization (S-C stretch) are indicated. The peaks marked (*) come from the PTFE substrate supporting the thin films. **d**, UV-vis absorbance curves for MoS_2 suspensions in SDS (blue curve) and 4-NBD functionalized MoS_2 (red curve). The A and B exciton peaks are labeled. The A peak redshifts after 4-NBD functionalization. **e**, Thermogravimetric analysis (TGA) mass loss curve for MoS_2 (blue curve) and 4-NBD functionalized MoS_2 (red curve). **f**, TGA derivative (DTG) curves for the mass loss curves in panel (e), showing dips corresponding to key mass loss components.

Optical absorbance spectra (UV-vis) were obtained for the re-dispersed samples (Figure 4.2d) which showed peaks at ~605 nm and ~660 nm attributed to the B and A excitonic transitions, respectively.[80] After functionalization, the B peak position remains the same while the A peak shifts toward longer wavelengths. While Eda et al.[111] have shown a redshift in both A and B peaks for thicker MoS_2 layers due to the change in band structure, we only see a redshift in the A peak, and we do not expect the functionalized MoS_2 to re-aggregate into thicker flakes because the 4-NBD groups prevent restacking. Instead, we postulate that the redshift can be attributed to electronic coupling of excitons to the conjugated aromatic groups attached to the MoS_2 surfaces. A similar exciton redshift has been observed for CdSe quantum dots coated in 4-mercaptobenzoic acid, which has a similar aromatic ring.[140] The increase in absorbance for functionalized MoS_2 below ~575 nm is attributed to absorbance of the attached organic groups.

Further characterization of the bulk MoS_2 dispersions with and without diazonium functionalization was conducted using thermogravimetric analysis (TGA) (see Experimental section for details). The TGA curves and first derivative curves are shown in Figure 4.2e and Figure 4.2f, respectively. The functionalized and unfunctionalized

MoS_2 both show a small mass loss below 100°C, which may be due to residual adsorbed water and other small molecules. There is also some mass loss below 200°C, which is more prominent for the functionalized MoS_2, that may be due to removal of van der Waals bonded molecules, similar to the observation of Knirsch et al.[127] for the functionalization of lithiated phase-transformed MoS_2. The diazonium salt by itself has a significant mass loss by about 160°C (see Appendix B, Figure B1), likely corresponding to a combination of sublimation and decomposition.

A sharp and prominent mass loss peak, corresponding to a mass loss of about 8%, occurs between 200°C to 300°C, with the maximum loss rate occurring at about 225°C. This sharp mass loss peak suggests the breaking of covalent bonds for species attached to the MoS_2 surface and the loss of nitrophenyl groups from the surface. There is also continued mass loss above 300°C, but it occurs at a faster rate, and with an additional peak at ~650°C and accelerating further above 800°C, which can be attributed to lattice degradation at higher temperatures. Using the total mass loss of the functionalized sample between 100°C and 450°C, which is about 15.7%, and using the molar masses of nitrobenzene and MoS_2, we estimate a surface coverage of about 24% assuming both sides of a monolayer MoS_2 flake in solution are available, or approximately 12% coverage on each side. This value is in direct agreement with the optimal concentration of ~8-12% predicted from DFT (calculations carried out by Elton J. G. Santos). This value is also comparable to the values estimated by Knirsch et al.[127] for the functionalization of lithium-treated phase-transformed MoS_2, which also showed the main mass loss due to

covalently attached groups occurring between about 200 to 450°C. Thus, we have achieved a similar degree of functionalization without the use of lithium treatment.

4.3.2. Protein attachment

MoS_2 is an attractive material for biological applications because it is biocompatible,[141] and it provides a large surface area for functionalization and for interaction with biomolecules, and its semiconducting properties enable MoS_2 to be used for biomolecule sensing via changes in charge transport or fluorescence. The large area and 2D nature of MoS_2 also provide the potential for its use in patterned arrays of devices for multiplexed detection schemes. Thus, examples of MoS_2 and TMDCs used in biological applications include bioimaging,[142] drug delivery and treatment,[64,142] and biosensing.[143] Previous studies have highlighted the excellent properties of MoS_2 for biosensing by incorporating it into field-effect transistors (FETs) that provided substantial sensitivity improvements over graphene-based devices[29] and, using gate dielectrics functionalized with protein antibodies, detection limits down to 60 fM concentrations.[144] However, direct covalent attachment of proteins to the MoS_2 has the potential to dramatically improve device sensitivity by bringing protein-analyte interactions to the semiconductor surface.[145] The ability to covalently tether active proteins to the surface of semiconducting MoS_2 thus represents a critical step to realizing the full biosensing potential of MoS_2. Accordingly, we developed a diazonium-based chemistry to tether fluorescent proteins[105,130] to the MoS_2 surface.

We first grafted carboxylic acid groups to the surface of mechanically exfoliated MoS_2 by functionalizing it with 4-carboxybenzenediazonium (4-CBD) tetrafluorobate (the UV-vis spectrum of bulk MoS_2 functionalized by 4-CBD is shown in the Appendix B, (Figure B2). The 4-CBD functionalized MoS_2 was then subsequently reacted to allow tethering of poly-histidine (His)-tagged green fluorescent protein (GFP) and the red fluorescent protein, mCherry (see Experimental section for protein synthesis and attachment details). The chemical attachment is schematically illustrated in Figure 4.3a. Although we used mechanically exfoliated MoS_2, as shown in the optical microscope image of Figure 4.3b, we expect the process to be compatible with liquid-phase exfoliated MoS_2 as well. AFM imaging of the pristine MoS_2 shows smooth atomic steps (Figure 4.3c). After protein attachment, AFM imaging (Figure 4.3d) shows a uniform increase in thickness (Figure 4.3e) that we interpret as a layer of proteins attached via the Ni-chelating linkage shown in the schematic, along with some pinholes consistent with those observed for 4-NBD attachment in Figure 4.3.

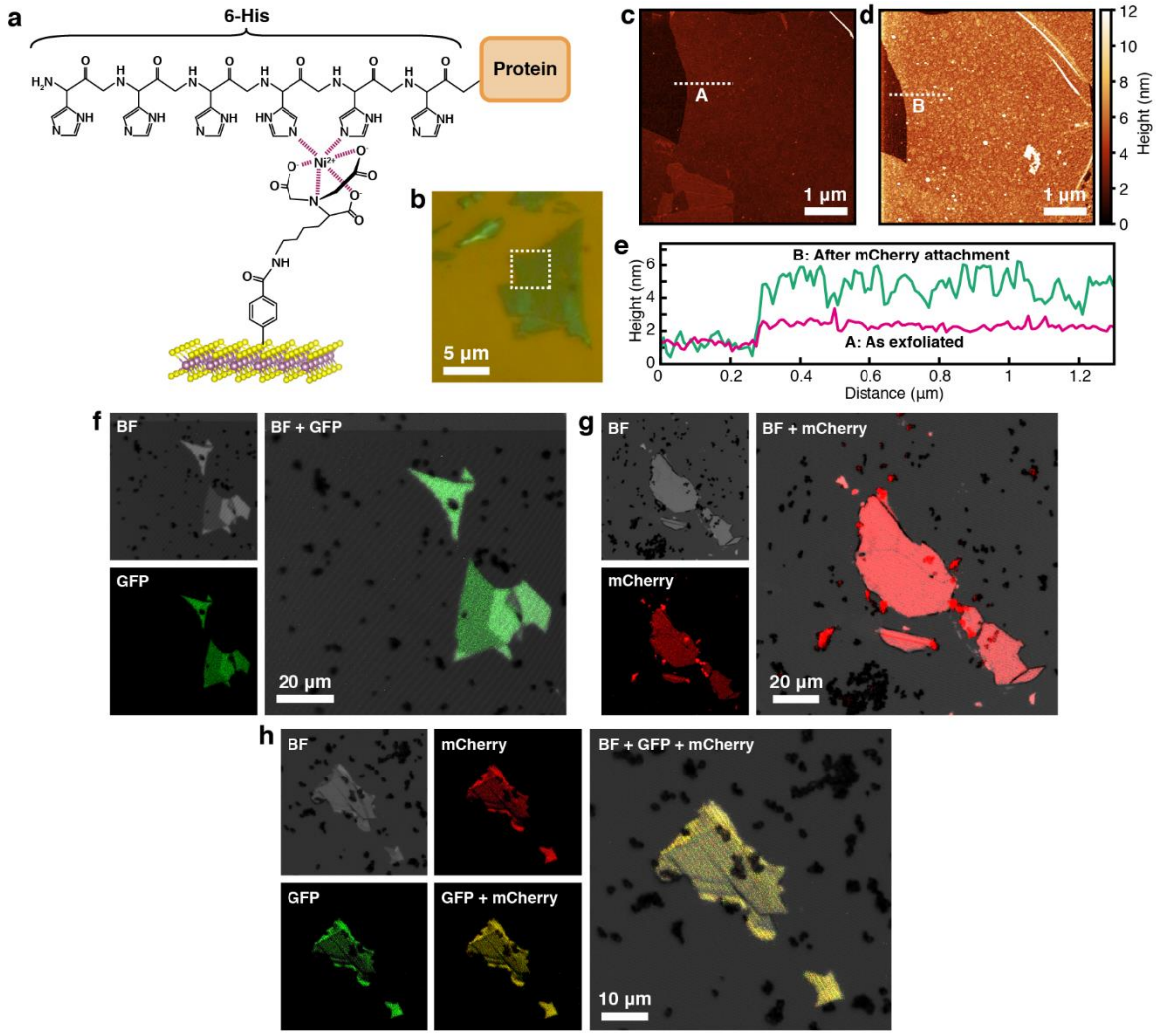

Figure 4.3| Attachment of active proteins to MoS_2. a, Schematic of NTA-Ni-chelation attachment of poly-histidine (His) tagged protein, linked to MoS_2 surface via diazonium functionalization chemistry. The diazonium salt used here was 4-carboxybenzene diazonium (4-CBD) tetrafluoroborate. **b**, Optical microscope image of mechanically exfoliated MoS_2 flakes featured in panels (c) and (d). **c**, AFM image of pristine MoS_2 in the region indicated by the dashed square in panel (b). **d**, AFM image in the same region as panel (c) after attachment of mCherry (red fluorescent protein) following initial 10 min functionalization with 4-CBD. **e**, Height profiles along lines A and B in panels (c) and (d). (f-h) Bright field (BF), confocal fluorescence microscopy images in GFP (green) and mCherry (red) channels, and fluorescence images overlaid onto BF images, after protein attachment process. **f**, GFP attachment. **g**, mCherry attachment. **h**, 1:1 mixture of GFP and mCherry attachment. In panels (f-h), fluorescence is only observed at the locations of the MoS_2 flakes where the initial diazonium functionalization has formed the anchors for the attachment chemistry as illustrated in the schematic.

To confirm attachment of active, viable proteins, we used confocal fluorescence microscopy to image the samples. Figures 4.3f-g show bright field optical images along with fluorescence images in the green and red channels for GFP and mCherry emission, respectively. These images indicate that the proteins have been successfully attached to the MoS_2 regions where the initial diazonium functionalization took place, and not in regions of the bare SiO_2/Si substrates. Furthermore, the strong fluorescence signals that we detect from the proteins demonstrate that our attachment chemistry is sufficiently gentle to avoid protein denaturation. Figure 4.3h shows the result of attaching a 1:1 mixture of GFP and mCherry. The overlay of both red and green channels on the bright field image, resulting in a combined yellow appearance, shows that both proteins have been uniformly localized to the MoS_2 flakes. Additional AFM and confocal images of more protein-functionalized samples are shown in Figure 4.4. In a control experiment where the diazonium functionalization step is skipped but all other processing steps are kept the same, no fluorescence is detected. Thus the covalent 4-CBD attachment step is crucial, and any possible association of the Ni^{2+} ions to the MoS_2 surface such as via coordination chemistry[138] is not sufficient to tether the proteins.

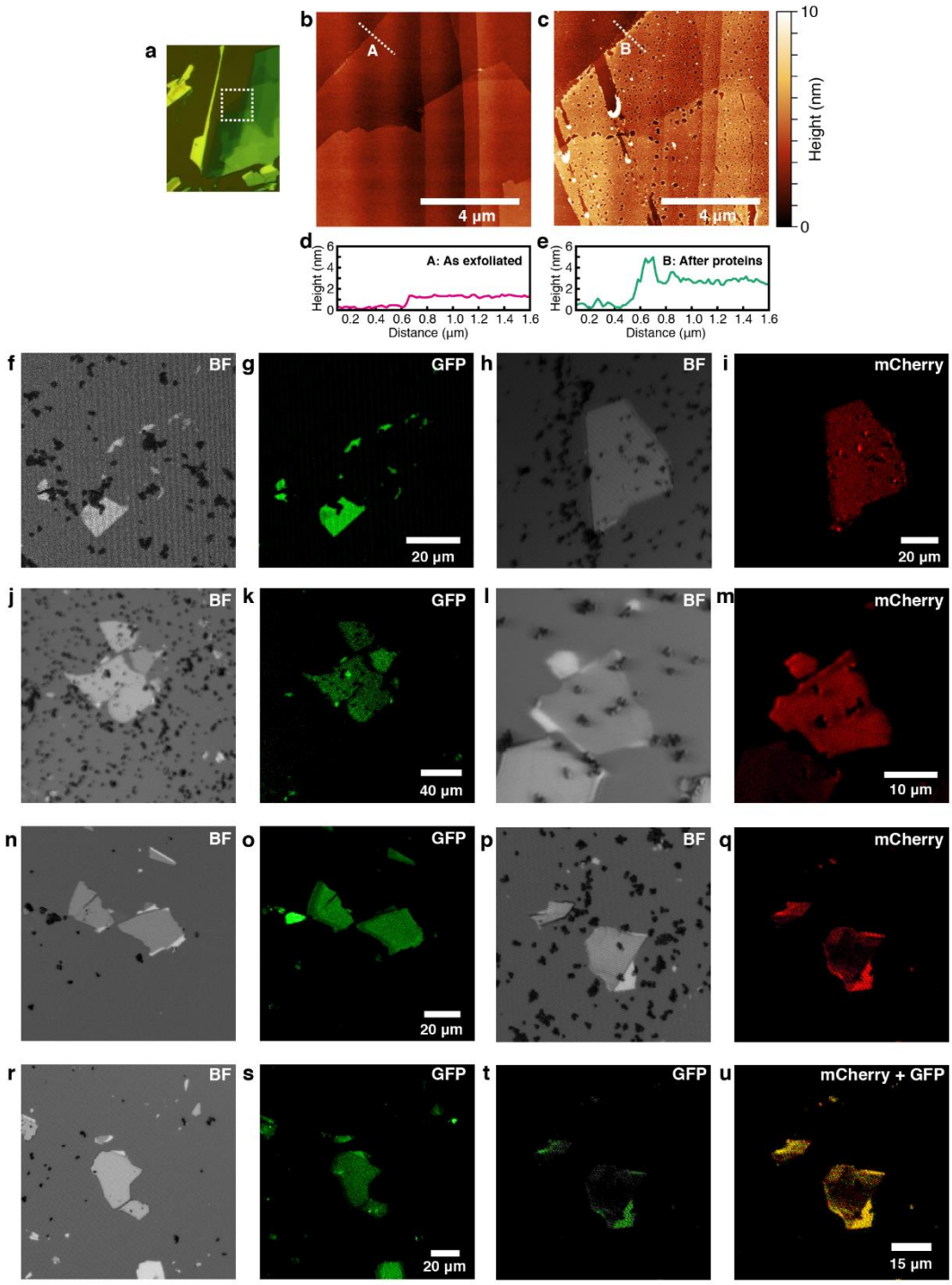

Figure 4.4| (a) Optical microscopy image of mechanically exfoliated MoS_2. (b,c) AFM images of the region marked by the dashed box in panel (a), (b) before and (c) after attachment of green fluorescent protein (GFP) with 2 h chemical functionalization with 4-carboxybenzenediazonium tetrafluoroborate. (d,e) Height profiles along lines A and B.

(f-g, j-k, n-o, r-s) Bright field and confocal fluorescence microscope images of MoS_2 after GFP attachment. (h-i, l-m) Bright field and confocal fluorescent microscope images of MoS_2 after mCherry attachment. (p-q, t-u) Bright field and fluorescence images of MoS_2 after attachment of a mixture of GFP and mCherry.

4.4. Conclusion

In conclusion, we have shown that pristine MoS_2 can be covalently functionalized with aryl diazonium salts without any harsh pretreatment. The covalent attachment was confirmed by FTIR and TGA. The peak for the A excitonic transition in optical absorbance spectrum of MoS_2 showed a red shift after functionalization which might be caused by the excitonic coupling of MoS_2 and the phenyl moiety. We also exploited the flexibility and robustness of the method to tether fluorescent proteins GFP and mCherry onto the mechanically exfoliated MoS_2 surface. We predict that this approach can be extended to tethering fluorescent proteins onto liquid-exfoliated MoS_2, enabling novel applications for these two-dimensional materials such as bar-coding of biomolecules for analysis of nucleic acids and proteins, which has previously been reported for quantum dots.[146]

Chapter 5

A General Approach to Drug Delivery Using Pristine Two-Dimensional Materials

5.1. Introduction

With the discovery of graphene in 2004, research in two-dimensional (2D) materials has grown exponentially. A variety of new 2D materials, such as boron nitride (BN) and transition metal dichalcogenides (TMDCs), have been synthesized since then. Different 2D materials have been shown to possess a wide range of properties. Graphene is a zero-bandgap material[6] with applications in transparent conductors;[147] MoS_2, the archetypal TMDC, is a direct bandgap semiconductor that shows photoluminescence;[112] and BN is a dielectric material[112]. Despite providing such a diverse set of properties, these 2D materials also possess multiple shared characteristics such as high surface-to-volume ratio, stability in aqueous environment, and susceptibility to various covalent and non-covalent functionalization techniques. Several 2D materials show low toxicities,[30,148,149] which combined with their high surface area makes them good candidates for applications such as drug delivery,[7,9,67,150,151] gene delivery,[11–13] and cell-labelling.[12,152]

Several studies have been published where the unique properties of 2D materials have been exploited for various applications in biosystems. In 2008, Sun et al. showed for the first time that PEGylated graphene oxide can be used to deliver drugs selectively into specific cancer cells.[153] Since then, several papers have used functionalized graphene and graphene-like materials for applications such as targeted drug delivery,[151] cellular imaging,[12] and photothermal therapy.[8] Apart from graphene and its derivatives, several

other 2D materials have been considered for this purpose. Weng et al. utilized porous, hydroxylated BN as biocompatible anticancer drug delivery vectors and showed that drug loaded on these nanocarriers exhibits greater potency than the free drug.[30] TMDCs have also been extensively used for delivering anticancer drugs and performing other combination therapies (see section 1.3.2). Upon careful inspection, one can notice that most of the studies carried out on drug delivery using two-dimensional materials have utilized covalent functionalization to modify their surface properties or utilized ion-intercalation methods to enhance the efficacy of the system. These additional modification steps not only add time and cost to the process, but some of them, such as lithiation, require the use of harsh conditions and toxic chemicals adding further complexity. Furthermore, few functionalization methods are known that can be utilized universally with all water-stable 2D materials necessitating the use of separate modification techniques for each material. An ideal strategy for preparing 2D material drug delivery vectors would be one that (i) utilizes pristine 2D materials, (ii) does not require covalent functionalization or harsh lithiation processes for dispersion or cell targeting, and (iii) is broadly applicable to a diverse set of 2D materials.

Here we report such a method that utilizes a common route to produce biocompatible dispersions of four different pristine 2D materials namely, MoS_2, $MoSe_2$, BN, and SnSe, and provides a general scheme for loading and delivery of anticancer drugs *in vitro*. To the best of our knowledge, two of these materials, $MoSe_2$ and SnSe, have never been used as drug delivery vectors previously. We used non-ionic polymer, F77, to disperse the above-mentioned materials and characterized these dispersions of

nanosheets in detail using UV-Visible spectroscopy (UV-Vis), transmission electron microscopy (TEM), atomic force microscopy (AFM), and inductively-coupled plasma mass spectrometry (ICP-MS). We used the MTT assay to assess the biocompatibility of the nanomaterial preparations. Next, we explored the adsorption behavior of doxorubicin (DOX), an anticancer drug, on all four materials and studied their drug delivery efficacy in HeLa cells. Finally, we show that adsorbing folic acid (FA) on the surface of $MoSe_2$ improves the potency of the system beyond that of just DOX itself by enabling targeted delivery to cells bearing folic acid receptors.

5.2. Results and Discussion

Ultrasonication of two-dimensional materials in surfactant solutions has been established as an efficient route for producing aqueous dispersions of pristine, unmodified nanosheets. In order to obtain biocompatible dispersions of the four materials we used pluronic F77, which is a linear, non-ionic block copolymer of polyethylene oxide (PEO) and polypropylene oxide (PPO). It contains a central hydrophobic region of PPO that is flanked on both sides by the hydrophilic PEO. Pluronics are a class of biocompatible polymers that have previously been shown to effectively disperse two-dimensional materials such as graphene, BN, and TMDCs.[154,155] The central PPO part of the polymer interacts with the basal plane of nanosheets through hydrophobic interaction and the hydrophilic PEO chains on the sides help stabilize it in water. Figure 5.1a shows a photograph of the dispersions of the four materials in F77 obtained after 30 mins of probe sonication of 0.6 g of bulk powder in 8 ml of 1% (w/v) F77 solution, followed by centrifugation at 21,130 rcf for 5 mins. The concentration of dispersions was determined

by ICP-MS. Optical absorbance spectrum of MoS_2 and $MoSe_2$ show their excitonic characteristic transitions; two peaks are observed between 620 nm and 670 nm for MoS_2 and two peaks observed at ~680 nm and ~789 nm for $MoSe_2$. SnSe and BN do not show any peaks in this region.

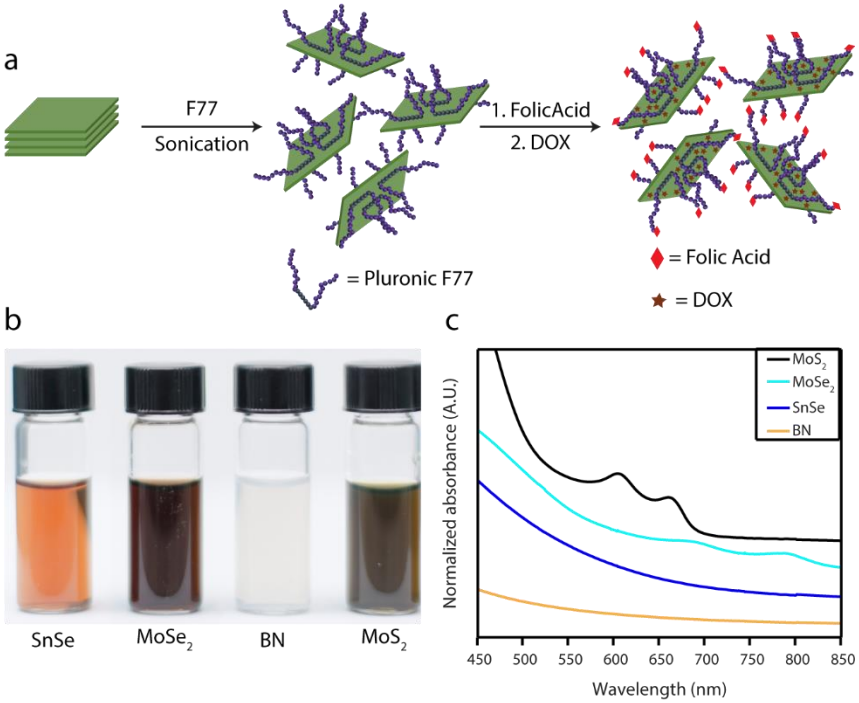

Figure 5.5 | Dispersing MoS_2, MoSe , BN, and SnSe in F77. a, Schematic showing dispersion of nanosheets in pluronic F77 and later adsorption of DOX. **b**, photograph of the dispersions in F77. **c**, Optical absorbance spectra of the four materials. Spectra are offset for clarity.

The obtained nanosheets were further characterized using TEM and AFM. TEM images in Figure 5.2a-5.2d confirm the two-dimensional nature of the nanosheets and show flakes that are between ~600 nm to ~2 μm in lateral dimension and possess different morphologies. Figure 5.2d-5.2f show AFM images of nanosheets of MoS_2, $MoSe_2$, and BN dispersed in F77 and the thickness of the flakes can be calculated to be between 5 nm to 7 nm overall.

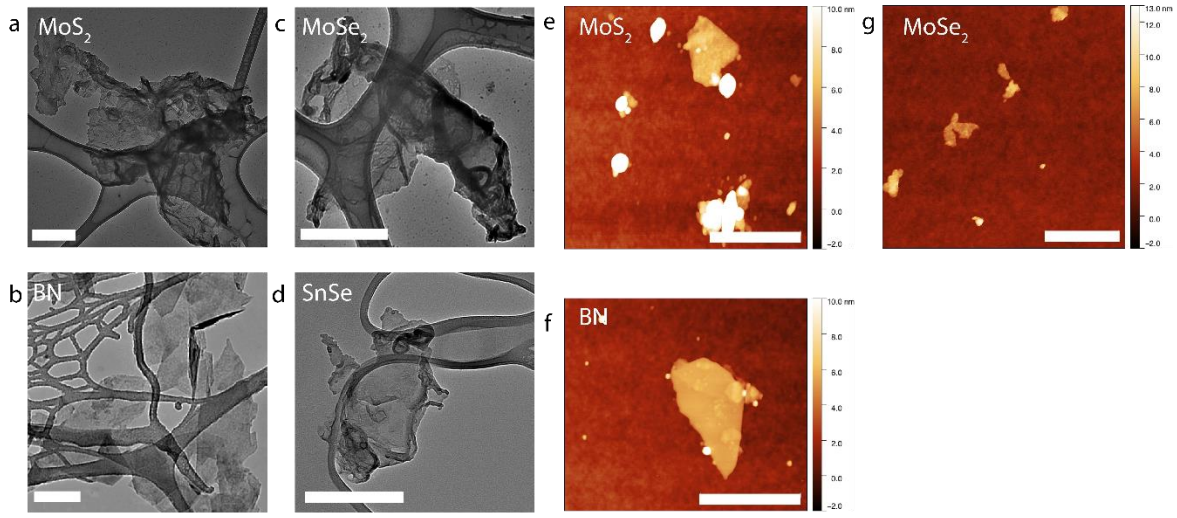

Figure 5.6 | Confirming 2D nature of the nanosheets. TEM images of **a**, MoS_2 **b**, BN **c**, $MoSe_2$ and **d**, SnSe in F77. AFM images of **e**, MoS_2, **f**, BN and **g**, $MoSe_2$ in F77. Scale bar is 300 nm.

Before these materials can be used for drug delivery, we need to determine their biocompatibility. This can be achieved by using the MTT assay, a colorimetric test that assesses cellular metabolic activity. For MTT testing, HeLa cells were pre-seeded on 96-well plates and allowed to grow for 24 hours. Then they were re-incubated with fresh medium (DMEM) and nanomaterial dispersions for another 24 hours. Subsequently the nanomaterial dispersions were replaced with MTT dye and incubated for another hour. The amount of formazan formed by reduction of MTT dye determines the relative cell viability, which can be measured by taking absorbance at 570 nm in a plate reader. From Figure 5.3a we can see that all four materials (MoS_2, $MoSe_2$, BN, and SnSe) are biocompatible, with relative cell viabilities over 95% even at concentrations as high as 100 μg/ml.

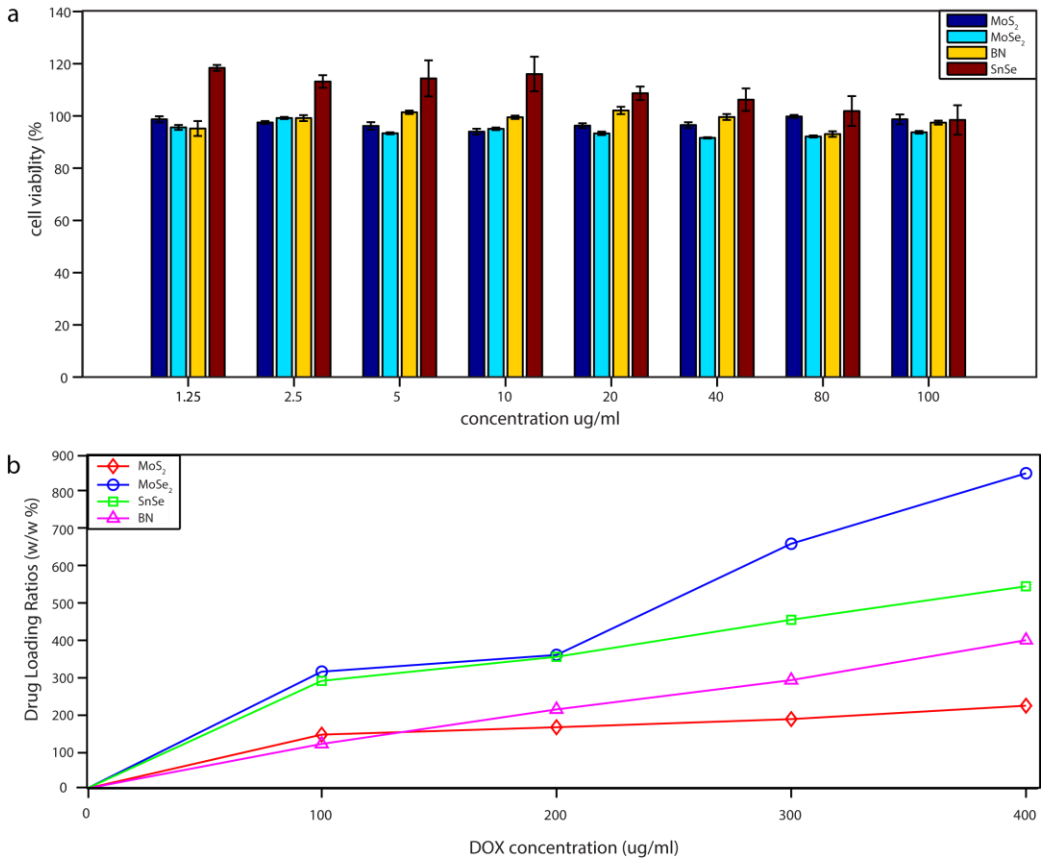

Figure 5.7 | Determining biocompatibility and drug loading capacity of the materials. a, Relative cell viability of HeLa cells with increasing concentration of respective two-dimensional materials. **b**, Loading ratios of DOX for all four materials as a function of DOX.

DOX, a widely used anticancer drug, was studied for delivery to cells via the 2D nanomaterials. DOX is an aromatic, hydrophobic drug that we hypothesized would absorb to the hydrophobic surfaces of the pristine 2D nanosheets. For loading the drug, dispersed nanomaterial was stirred with increasing concentrations of DOX at pH 7.4 for 24 hours and then filtered and rinsed to remove any unbound drug. Since DOX has a number clearly defined absorbance peaks, optical absorbance spectroscopy was used to determine the drug loading ratios on MoS_2, $MoSe_2$, BN, and SnSe. Figure 5.3b shows how the drug loading ratios increase as a function of DOX concentration. The highest

loading (w/w %) obtained for MoS_2, $MoSe_2$, BN, and SnSe was 223%, 850%, 400%, and 545% respectively. Such high drug loading is a direct consequence of the high surface area to volume ratios of two-dimensional materials and the hydrophobic interactions between DOX and the nanosheets. Higher DOX loading ratios were not possible as the drug is not stable in an aqueous environment at concentrations higher than those used in this study.

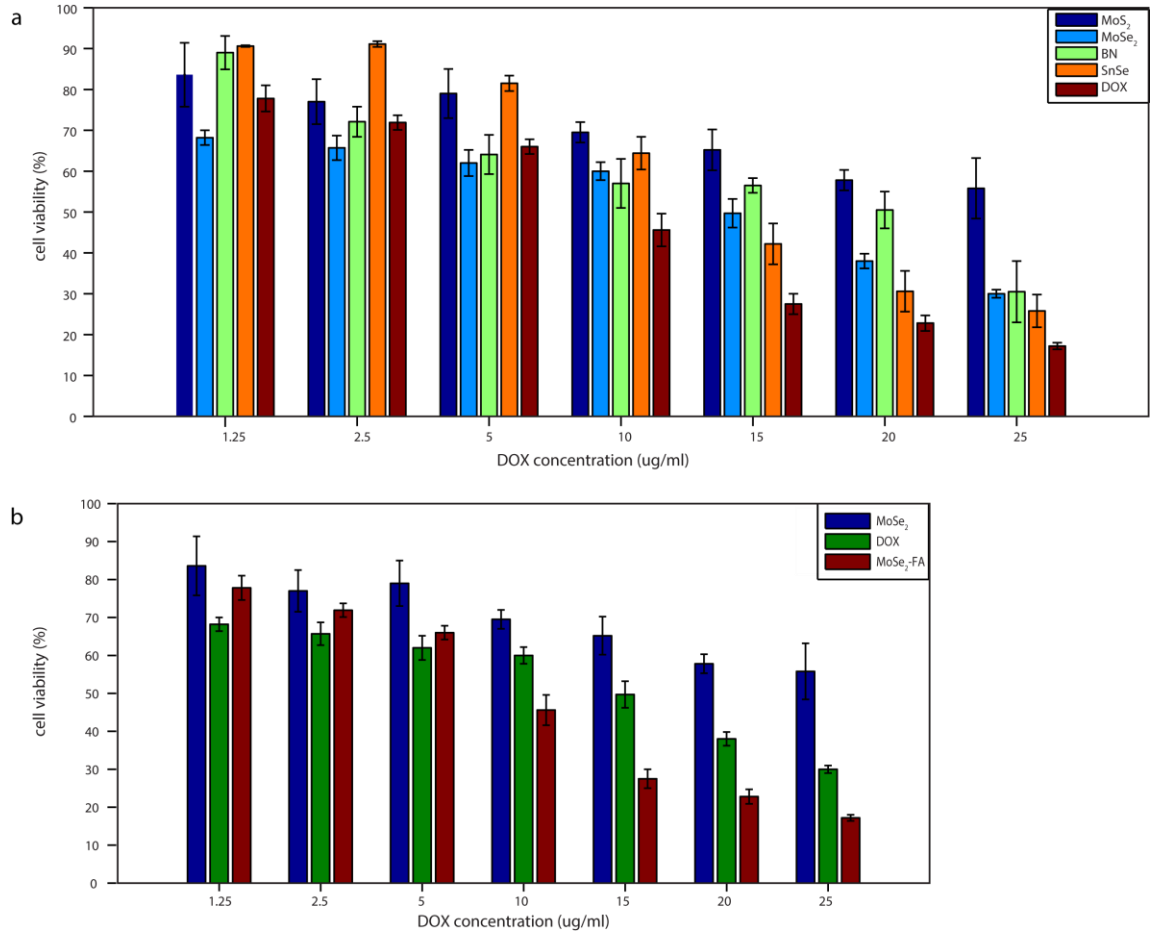

Figure 5.8 | Determining the drug delivery efficacy of MoS_2, $MoSe_2$, BN, and SnSe. **a**, Relative cell viability as a function of DOX concentration delivered to the cells. **b**, Comparison of cell viabilities of free DOX, $MoSe_2$ without folic acid and $MoSe_2$ with folic acid.

After establishing the biocompatibility of the nanomaterials and determining their drug-loading capacity, we determined their efficacy against HeLa cells, which is a cervical cancer cell line. For this purpose, HeLa cells were pre-seeded in 96-well plates at $3x10^4$ cells per well and allowed to grow for 24 hours. Then, the cells were incubated with nanomaterial-DOX dispersions for 1 hour and finally, the cell viability was determined using MTT assay as described above. Cell viabilities at 25 μg/ml, the highest concentration of DOX used, were 56%, 30%, 31%, 26%, and 17% for MoS_2, $MoSe_2$, BN, SnSe, and free DOX (see Figure 5.4a). The killing efficiency of $MoSe_2$, BN, and SnSe, although quite high, is still less than that of free DOX.

In an attempt to increase the overall efficacy of the system, we conjugated folic acid to F77 and then dispersed the nanomaterials in the modified surfactant. HeLa cells over-express folate receptors on the surface and docking folic acid on the surface of nanosheets increases the interaction between the cell surface and nanosheets resulting in an improved therapeutic efficiency. We used $MoSe_2$ as the model material for this experiment. The supramolecular complex of $MoSe_2$, F77, folic acid, and DOX shows a much higher killing efficiency than $MoSe_2$ (30%) or even free DOX (17%) itself as shown in Figure 5.4b. The simple supramolecular chemistry renders the need for covalent functionalization or lithiation of the nanosheets unnecessary greatly simplifying the process.

5.3. Conclusion

In conclusion, we have developed a generalizable strategy that can be used for targeted delivery of anticancer drugs with a variety of different two-dimensional

materials: MoS_2, $MoSe_2$, BN, and SnSe. We exploited high surface area and hydrophobic nature of the nanosheets to dock DOX and folic acid on their surface to achieve therapeutic efficiency higher than that of free DOX itself. The lack of complicated covalent functionalization or lithiation steps in the methodology simplifies the process and allows for a more generalizable approach towards targeted drug delivery using two-dimensional materials. Our approach can potentially be used with any water-stable, hydrophobic two-dimensional material while eliminating the need for covalent modifications.

5.4. Materials and Methods

5.4.1. Preparation and characterization of nanomaterial dispersions.

0.6 g of MoS_2, $MoSe_2$, BN, and SnSe were added to 15 ml centrifuge tubes and probe sonicated (Branson Digital Sonifier 450D, 4 mm tip) in 8 ml of 1% (w/v) aqueous solution of Pluronic F77 for 30 mins at 20% amplitude corresponding to a power output of 11-13 W. The resulting dispersions were transferred to 1.5 ml centrifuge tubes and centrifuged at 21130 rcf for 5 mins except BN which was centrifuged at 500 rcf for 10 mins.

To acquire UV-Vis spectra, the dispersions were diluted with water as needed the spectra were collected from 400 nm to 850 nm against a blank of reference of F77 solution in a Jasco V670 UV-Vis-NIR spectrophotometer. TEM samples were prepared by dropping above dispersions on holey (400 mesh Cu, Ted Pella Inc.) TEM grids with an ultrathin carbon layer and the images were collected on Philips CM 12 at 80 kV. AFM imaging was carried out on a Multimode V system (Bruker Corp.) with ScanAsyst-Air

tips (Bruker) in ScanAsyst non-contact mode. Gwyddion was used to process AFM images. AFM samples were prepared by spin-coating the dispersion on a SiO_2/Si substrate at 3000 rpm for 1 min. Spin coating was repeated several times to increase density of the nanosheets on the substrate. All AFM images were collected by Ximo S. Chu.

5.4.2. Determining Cytotoxicity of Nanomaterials

MTT assay was employed to determine the cytotoxicity of MoS_2, $MoSe_2$, BN, and SnSe dispersions in F77. All dispersions were prepared by the above-mentioned method except that the sonication time was increased to 2 hours to decrease size of flakes. Then, HeLa cells were pre-seeded on 96 well plates at a concentration of $3x10^4$ cells per well and these were allowed to grow for 24 hours in DMEM. Then these were incubated with the nanomaterial dispersions and fresh medium for another 24 hours and finally the nanomaterial dispersions were replaced with MTT solution in dimethyl sulfoxide (DMSO) and incubated for another hour. Wells with more number of viable cells showed a brighter purple color and the relative cell viabilities were determined by measuring optical absorbance at 570 nm in a plate reader.

5.4.3. Drug Loading

For DOX loading, pluronic dispersed nanomaterials were stirred with different concentrations of doxorubicin at pH = 7.4. The mixture was stirred for 24 hours and the excess unbound DOX was washed away by filtering the solution through 100 kDa filter and rinsing with water multiple times. The concentration of DOX on the nanosheets was

determined using a custom MATLAB deconvolution algorithm. Drug loading experiments were carried out by Abhishek Debnath.

5.4.4. *In-vitro* Cellular Uptake of DOX-Loaded Nanosheets

To study the drug delivery uptake, Hela cells were pre-seeded in 96 well plates at $3x10^4$ cells per well and allowed to grow for 24 hours. The cells were incubated with drug-laden nanomaterial for 1 hours. The nanomaterial dispersions were pipetted out and the wells were washed twice with PBS and re-incubated with DMEM for 24 hours. MTT assay was used to determine relative cell viabilities using the same protocol as mentioned above. Folic-acid-modified F77 (F77-FA) was synthesized using method similar to one reported by Liu et al.[67] and the same process was repeated with F77-FA as used with F77 alone. Abhishek Debnath assisted with these experiments.

Chapter 6

Summary and Future Outlook

6.1. Thesis Summary

In this thesis, I have demonstrated that ultrasonication-mediated liquid-phase exfoliation can be used to produce two-dimensional metal diborides: a new class of boron-rich materials. Two-dimensional metal diborides were completely characterized using bulk and nanoscale techniques including optical absorbance spectroscopy, transmission electron microscopy (TEM), and electron energy loss spectroscopy. I also showed that two-dimensional chromium diboride can be incorporated in polyvinyl alcohol (PVA) and possesses superior mechanical reinforcement capability compared to other well-known two-dimensional materials such as graphene and molybdenum disulfide.

Metal diborides exhibit varying dispersion behavior in different organic solvents. This can be explained in terms of Hansen solubility parameters and surface energy of the nanosheets. Calculation of these fundamental dispersion parameters helps us understand the dispersion process, predicts new and efficient solvents that can disperse these materials, and helps identify ideal solvents for specific applications. For instance, in the preparation of new metal diboride composites, it is essential to know the organic solvents that can solubilize the polymer and effectively disperse the 2D metal diboride nanosheets.

Ultrasonication can also be used to disperse other two-dimensional materials, such as transition metal dichalcogenides (TMDCs). MoS_2, the archetypal TMDC, was dispersed and then chemically modified with ultrasonication-mediated diazonium

chemistry. This method provides a direct route for functionalization of pristine MoS_2, rendering lithium-based treatments unnecessary. Detailed density functional theory (DFT) calculations, supported by careful experimentation, suggest that the reaction proceeds through a mixture of surface defects and cooperative effects with surface-bound molecules. Furthermore, the process is quite robust and can be used to tether active proteins on the surface, making it amenable to various biosensing applications.

The large surface-area-to-volume ratio and nanoscale dimensions that are commensurate with dimensions of biological components make two-dimensional materials attractive candidate for applications such as drug delivery, gene delivery, and bioimaging. Dispersions of pristine two-dimensional materials, such as MoS_2, $MoSe_2$, BN, and SnSe, in F77 – a non-ionic, biocompatible polymer – can be used to efficiently load anticancer drug DOX on their surface. Remarkably, the amount of DOX loaded on the nanosheets can be several times more than their own mass, making them effective drug delivery vectors. The F77 polymer can be further conjugated with folic acid (FA) which increases the interaction between HeLa cells and the $MoSe_2$-F77-FA-DOX supramolecular complex rendering it more potent than free DOX itself. As this process does not require any covalent modification of the nanomaterials, it can be generalized to achieve drug delivery with a variety of two-dimensional materials belonging to different classes and eliminates the toxicity and processing drawbacks associated with covalently modified or phase-engineered 2D nanosheets.

6.2. Future Directions

6.2.1. Towards 3D Printing of High-Temperature Ceramics and Superconductors

The ability to disperse high-temperature ceramics, such as TiB_2, ZrB_2, and HfB_2, with melting temperatures above 2700^oC in liquids can provide a remarkable method for easy processing of such materials. Dispersions of MgB_2, a well-known superconductor in bulk form, may also be used to provide an alternative route for its processing. The liquid-dispersed metal diborides can potentially be spray coated or inkjet-printed to make coatings and patterns of ceramics on surfaces. Furthermore, these dispersions may be incorporated in polymers for 3D printing. Figure 6.1 shows composites of polymer PR48 made with dispersed magnesium diboride and titanium diboride. These composites are homogenous and can be prepared by using a simple desktop stereolithography system (Autodesk Ember 3D Printer). 3D-printed composites of metal diborides can also be made with biocompatible polymers such as poly(ethylene glycol) diacrylate (PEGDA). The ease of dispersing metal diborides accompanied with the knowledge of their dispersion behavior in various solvents can lead towards novel applications such as 3D printed ultra-high temperature ceramics and superconductors.

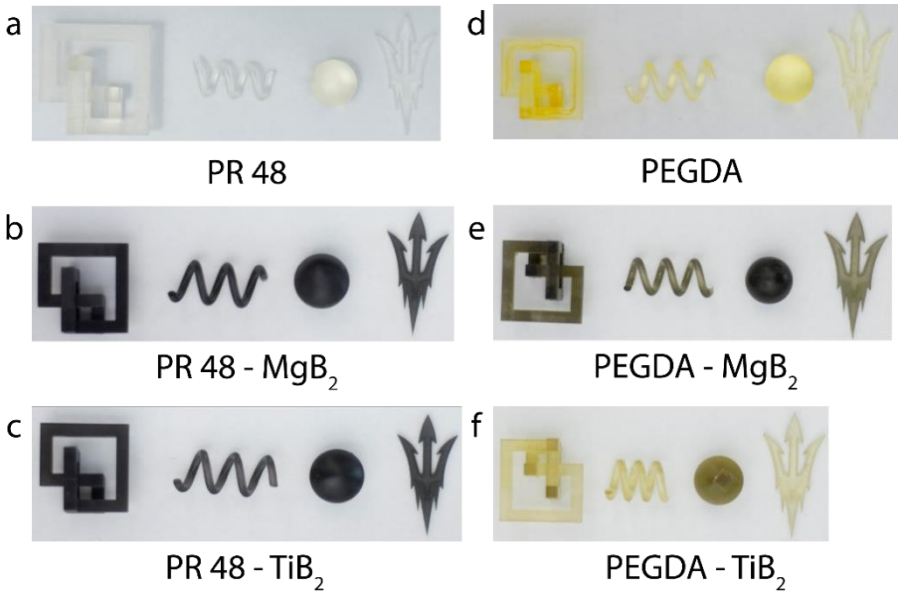

Figure 6.9 | 3D printed polymer composites of metal diborides. a-c, 3D prints with PR48 photocurable polymer. **d-f**, 3D prints with PEGDA photocurable polymer.

6.2.2. Biosensors and *In-Vivo* Targeted Drug Delivery

Diazonium functionalization of MoS_2 opens it up to various biosensing applications. Future studies can involve detection of biomarkers of various diseases by using antibody-functionalized MoS_2-based sensors. Similar diazonium chemistries may also be exploited to tune chemical, electronic, and optoelectronic properties of other pristine TMDCs which can lead to a whole array of materials with tunable properties.

Furthermore, the efficacy of the drug delivery system reported here may further be established by conducting *in vivo* studies and expanding the range of usable two-dimensional materials. More detailed studies into the biodegradability of these drug delivery vectors and their ultimate fate in the body must to be conducted before these materials can be used to treat cancer in humans.

Bibliography

1. Raimond, J. M., Brune, M., Computation, Q., Martini, F. De & Monroe, C. Electric Field Effect in Atomically Thin Carbon Films. *Science.* **306,** 666–670 (2004).

2. Reich, S., Maultzsch, J., Thomsen, C. & Ordejo, P. Tight-binding description of graphene. *Phys. Rev. b* **66,** 1–5 (2002).

3. Nakada, K., Fujita, M., Dresselhaus, G. & Dresselhaus, M. S. Edge state in graphene ribbons : Nanometer size effect and edge shape dependence. *Phys. Rev. b* **54,** 954–961 (1996).

4. Lee, C., Wei, X., Kysar, J. W. & Hone, J. Measurmeent of the Elastic Properties and Intrinsic Strength of Monolayer Graphene. *Science.* **321,** 385–389 (2008).

5. Geim, A. K. Graphene : Status and Prospects. *Science.* **324,** 1530–1535 (2009).

6. A.K. Geim and K. S. Novoselov. The rise of graphene. *Nat. Mater.* **6,** 183–191 (2007).

7. Kunping Liu, Jing-Jing Zhang, Fang-Fang Cheng, Ting-Ting Zheng, C. W. and J.-J. Z. Green and facile synthesis of highly biocompatible graphene nanosheets and its application for cellular imaging and drug delivery. *J. Mater. Chem.* **21,** 12034–12040 (2011).

8. Robinson, J. T. *et al.* Ultrasmall Reduced Graphene Oxide with High Near-Infrared Absorbance for Photothermal Therapy. *J. Am. Chem. Soc.* **133,** 6825–6831 (2011).

9. Sun, X. *et al.* Nano-Graphene Oxide for Cellular Imaging and Drug Delivery. *Nano Res* **1,** 203–212 (2008).

10. Rana, V. K. *et al.* Synthesis and Drug-Delivery Behavior of Chitosan-Functionalized Graphene Oxide Hybrid Nanosheets. *Macromol. Mater. Eng.* 131–140 (2011). doi:10.1002/mame.201000307

11. Feng, L. *et al.* Polyethylene glycol and polyethylenimine dual-functionalized nano-graphene oxide for photothermally enhanced gene delivery. *Small* **9,** 1989–1997 (2013).

12. Kim, H., Namgung, R., Singha, K., Oh, I.-K. & Kim, W. J. Graphene oxide–polyethylenimine nanoconstruct as a gene delivery vector and bioimaging tool. *Bioconjug. Chem.* **22,** 2558–2567 (2011).

13. Chen, B. *et al.* Polyethylenimine-functionalized graphene oxide as an efficient gene delivery vector. *J. Mater. Chem.* **21,** 7736–7741 (2011).

14. Peng, C., Hu, W., Zhou, Y., Fan, C. & Huang, Q. Intracellular Imaging with a Graphene-Based Fluorescent Probe. *Small* **6,** 1686–1692 (2010).

15. Zhang, B., Li, Q. & Cui, T. Biosensors and Bioelectronics Ultra-sensitive suspended graphene nanocomposite cancer sensors with strong suppression of electrical noise. *Biosens. Bioelectron.* **31,** 105–109 (2012).

16. Abajo, F. J. G. De, Pruneri, V. & Altug, H. Mid-infrared plasmonic biosensing with graphene. *Science.* **349,** 165–168 (2015).

17. Xu, M., Liang, T., Shi, M. & Chen, H. Graphene-Like Two-Dimensional Materials. *Chem. Rev.* **113,** 3766–3798 (2013).

18. Dávila, M. E., Xian, L., Cahangirov, S., Rubio, A. & Lay, G. Le. Germanene : a novel two-dimensional germanium allotrope akin to graphene and silicene Germanene : a novel two-dimensional germanium allotrope akin to graphene and silicene. *New J. Phys.* **16,** 1–10 (2014).

19. Yuhara, J. *et al.* Large area planar stanene epitaxially grown on Ag(111). *2D Mater.* **5,** 1–8 (2018).

20. Ye, P. D. *et al.* Phosphorene : An Unexplored 2D Semiconductor with a High Hole. *ACS Nano* 4033–4041 (2014).

21. Kang, J. *et al.* Solvent Exfoliation of Electronic-Grade , two-dimensional black phosphorus. *ACS Nano* **9,** 3596–3604 (2015).

22. Mannix, A. J. *et al.* Synthesis of borophenes: Anisotropic two-dimensional polymorphs. *Science.* **350,** 1513–1516 (2015).

23. Lei Liu, Jewook Park, David A. Siegel, Kevin F. McCarty, Kendal W. Clark, Wan Deng, Leonardo Basile, Juan Carlos Idrobo, An-Ping Li, G. G. Heteroepitaxial Growth of Two-Dimensional Hexagonal Boron Nitride Templated by Graphene Edges. *Science.* **343,** 163–168 (2014).

24. Naguib, M., Mochalin, V. N., Barsoum, M. W. & Gogotsi, Y. 25th Anniversary Article : MXenes : A New Family of Two-Dimensional Materials. *Adv. Mater.* **26,** 992–1005 (2013).

25. Wang, Q. H., Kalantar-zadeh, K., Kis, A., Coleman, J. N. & Strano, M. S.

Electronics and optoelectronics of two-dimensional transition metal dichalcogenides. *Nat. Nanotechnol.* **7,** 699–712 (2012).

26. Yin, Z. *et al.* Single-layer MoS2 phototransistors. *ACS Nano* **6,** 74–80 (2011).

27. Wang, N. *et al.* Synthesis of Strongly Fluorescent Molybdenum Disul fi de Nanosheets for Cell-Targeted Labeling. *ACS Appl. Mater. Interfaces* **6,** 19888–19894 (2014).

28. Bang, G. S. *et al.* Effective Liquid-Phase Exfoliation and Sodium Ion Battery Application of MoS2 Nanosheets. *ACS Appl. Mater. Interfaces* **6,** 7084–7089 (2014).

29. Sarkar, D. *et al.* MoS2 field-effect transistor for next-generation label-free biosensors. *ACS Nano* **8,** 3992–4003 (2014).

30. Weng, Q. *et al.* Highly water-soluble, porous, and biocompatible boron nitrides for anticancer drug delivery. *ACS Nano* **8,** 6123–6130 (2014).

31. Son, Y. *et al.* Layer number dependence of MoS2 photoconductivity using photocurrent spectral atomic force microscopic imaging. *ACS Nano* **9,** 2843–2855 (2015).

32. Tsai, M. L. *et al.* Monolayer MoS2 heterojunction solar cells. *ACS Nano* **8,** 8317–8322 (2014).

33. Kalantar-zadeh, K. *et al.* Two-Dimensional Transition Metal Dichalcogenides in Biosystems. *Adv. Funct. Mater.* **25,** 5086–5099 (2015).

34. May, P., Khan, U., O'Neill, A. & Coleman, J. N. Approaching the theoretical limit for reinforcing polymers with graphene. *J. Mater. Chem.* **22,** 1278 (2012).

35. Cao, Y. *et al.* Unconventional superconductivity in magic-angle graphene superlattices. *Nature* (2018).

36. Butler, S. Z. *et al.* Opportunities in Two-Dimensional Materials Beyond Graphene. *ACS Nano* **7,** 2898–2926 (2013).

37. Li, X. *et al.* Large-Area Synthesis of High-Quality and Uniform Graphene Films on Copper Foils. *Science.* **3893,** 1312–1315 (2009).

38. Jaeho Jeon, Sung Kyu Jang, Su Min Jeon, Gwangwe Yoo, Yun Hee Jang, J.-H. P. and S. L. Layer-controlled CVD growth of large-area two-dimensional MoS2 film. *Nanoscale* **7,** 1688–1695 (2015).

39. Kobayashi, T., Bando, M., Kimura, N., Shimizu, K. & Kadono, K. Production of a 100-m-long high-quality graphene transparent conductive film by roll-to-roll chemical vapor deposition and transfer process. *Appl. Phys. Lett.* **102,** 1–5 (2013).

40. Nicolosi, V., Chhowalla, M., Kanatzidis, M. G., Strano, M. S. & Coleman, J. N. Liquid Exfoliation of Layered Materials Liquid Exfoliation of Layered Materials. *Science.* **340,** (2013).

41. Pati, S. K. & Rao, C. N. R. MoS2 and WS2 Analogues of Graphene. *Angew. Chem. Int. Ed.* **49,** 4059–4062 (2010).

42. Smith, R. J. *et al.* Large-Scale Exfoliation of Inorganic Layered Compounds in Aqueous Surfactant Solutions. *Adv. Mater.* **23,** 3944–3948 (2011).

43. Coleman, J. N. *et al.* Two-Dimensional Nanosheets Produced by Liquid Exfoliation of Layered Materials. *Science.* **331,** 568–571 (2011).

44. Lotya, M. *et al.* Liquid Phase Production of Graphene by Exfoliation of Graphite in Surfactant / Water Solutions. *J. Am. Chem. Soc.* **131,** 3611–3620 (2009).

45. Hernandez, Y., Lotya, M., Rickard, D., Bergin, S. D. & Coleman, J. N. Measurement of Multicomponent Solubility Parameters for Graphene Facilitates Solvent Discovery. *Langmuir* **3,** 3208–3213 (2010).

46. Cunningham, G. *et al.* Solvent Exfoliation of Transition Metal Dichalcogenides : Dispersability of Exfoliated Nanosheets Varies Only Weakly Between Compounds Solvent Exfoliation of Transition Metal Dichalcogenides : Dispersability of Exfoliated Nanosheets Varies Only Weakly Bet. *ACS Nano* **6,** 3468–3480 (2012).

47. Suk, J. W. *et al.* Transfer of CVD-Grown Monolayer Graphene onto Arbitrary Substrates. *ACS Nano* **5,** 6916–6924 (2011).

48. Mak, K. F., Lee, C., Hone, J., Shan, J. & Heinz, T. F. Atomically Thin MoS 2 : A New Direct-Gap Semiconductor. *Phys. Rev. Lett.* **136805,** 1–4 (2010).

49. Intel ' s 10 nm Technology : Delivering the Highest Logic Transistor Density in the Industry Through the Use of Hyper Scaling. (2017). Available at: https://newsroom.intel.com/newsroom/wp-content/uploads/sites/11/2017/09/10-nm-icf-fact-sheet.pdf.

50. Radisavljevic, B., Radenovic, A., Brivio, J., Giacometti, V. & Kis, A. Single-layer MoS2 transistors. *Nat. Nanotechnol.* **6,** 147–50 (2011).

51. Wang, H. *et al.* Integrated Circuits Based on Bilayer MoS 2 Transistors. *Nano Lett.* **12,** 4674–4680 (2012).

52. Qiu, H. *et al.* Electrical characterization of back-gated bi-layer MoS2 field-effect transistors and the effect of ambient on their performances. *Appl. Phys. Lett.* **100,** 1–3 (2012).

53. Liu, W., Kang, J. & Cao, W. High-Performanc Few-Layer MoS2 Fieldd-Effect-Transistor with Record Low Contact-Resistance. *IEEE Int.* **19,** 499–502 (2013).

54. Larentis, S., Fallahazad, B. & Tutuc, E. Field-effect transistors and intrinsic mobility in ultra-thin MoSe2 layers Field-effect transistors and intrinsic mobility in ultra-thin MoSe 2 layers. *Appl. Phys. Lett.* **101,** 1–4 (2012).

55. Hwang, W. S. *et al.* room temperature modulation and ambipolar behavior Transistors with chemically synthesized layered semiconductor WS2 exhibiting 10 5 room temperature modulation and ambipolar behavior. *Appl. Phys. Lett.* **101,** 1–4 (2012).

56. Das, S. & Appenzeller, J. WSe2 field effect transistors with enhanced ambipolar characteristics. *Appl. Phys. Lett.* **103,** 1–5 (2013).

57. Gong, Y. *et al.* Vertical and in-plane heterostructures from WS2 /MoS2 monolayers. *Nat. Mater.* **13,** 1135–1142 (2014).

58. Hong, X. *et al.* Ultrafast charge transfer in atomically thin MoS2/WS2 heterostructures. *Nat. Nanotechnol.* **9,** 682–686 (2014).

59. Pospischil, A., Furchi, M. M. & Mueller, T. Solar-energy conversion and light emission in an atomic monolayer p-n diode. *Nat. Nanotechnol.* **9,** 257–261 (2014).

60. Cheng, R. *et al.* Electroluminescence and photocurrent generation from atomically sharp WSe2/MoS2heterojunction p-n diodes. *Nano Lett.* **14,** 5590–5597 (2014).

61. Choi, W. *et al.* High-detectivity multilayer MoS2 phototransistors with spectral response from ultraviolet to infrared. *Adv. Mater.* **24,** 5832–5836 (2012).

62. Wang, X. *et al.* Differences in the Toxicological Potential of 2D versus Aggregated Molybdenum Disulfi de in the Lung. *Small* **11,** 5079–5087 (2015).

63. Chou, S. S. *et al.* Chemically Exfoliated MoS2 as Near-Infrared Photothermal Agents. *Angew. Chemie* **22904,** 4254–4258 (2013).

64. Cheng, L. *et al.* PEGylated WS2 Nanosheets as a Multifunctional Theranostic

Agent for in vivo Dual-Modal CT / Photoacoustic Imaging Guided Photothermal Therapy. *Adv. Mater.* **26,** 1886–1893 (2014).

65. Liu, T. *et al.* Combined photothermal and photodynamic therapy delivered by PEGylated MoS 2 nanosheets †. *Nanoscale* **6,** 11219–11225 (2014).

66. Yong, Y. *et al.* combined photodynamic and photothermal therapy of cancer cells. *Nanoscale* **6,** 10394–10403 (2014).

67. Liu, T. *et al.* Drug Delivery with PEGylated MoS2 Nano-sheets for Combined Photothermal and Chemotherapy of Cancer. *Adv. Mater.* **26,** 3433–3440 (2014).

68. Liu, T. *et al.* Iron Oxide Decorated MoS2 Nanosheets with Double PEGylation for Chelator-Free Radiolabeling and Multimodal Imaging Guided Photothermal Therapy. *ACS Nano* **9,** 950–960 (2015).

69. Kim, J., Kim, H. & Kim, W. J. Single-Layered MoS2 – PEI – PEG Nanocomposite- Mediated Gene Delivery Controlled by Photo and Redox Stimuli. *Small* **12,** 1184–1192 (2015).

70. Vajeeston, P., Ravindran, P., Ravi, C. & Asokamani, R. Electronic structure , bonding , and ground-state properties of AlB2 -type transition-metal diborides. *Phys. Rev. b* **63,** 45115 (2001).

71. Nishibori, E. *et al.* Bonding nature in MgB2. *J. Phys. Soc. Japan* **70,** 2252–2254 (2001).

72. Wagner, F. R., Baranov, A. I., Grin, Y. & Kohout, M. A Position-Space View on Chemical Bonding in Metal Diborides with AlB2 Type of Crystal Structure. *Zeitschrift für Anorg. und Allg. Chemie* **639,** 2025–2035 (2013).

73. Buzea, C. & Yamashita, T. Review of the superconducting properties of MgB 2. *Supercond. Sci. Technol.* **14,** R115 (2001).

74. Munro, R. G. Material Properties of Titanium Diboride. *J. Res. Natl. Inst. Stand. Technol.* **105,** 709–720 (2000).

75. Fahrenholtz, W. G., Hilmas, G. E., Talmy, I. G. & Zaykoski, J. A. Refractory diborides of zirconium and hafnium. *J. Am. Ceram. Soc.* **90,** 1347–1364 (2007).

76. Gu, Q., Krauss, G. & Steurer, W. Transition metal borides: Superhard versus ultra-incompressible. *Adv. Mater.* **20,** 3620–3626 (2008).

77. Šimůnek, A. Anisotropy of hardness from first principles: The cases of ReB2 and

OsB2. *Phys. Rev. B - Condens. Matter Mater. Phys.* **80,** 1–4 (2009).

78. Amsler, M., Botti, S., Marques, M. A. L. & Goedecker, S. Conducting Boron Sheets Formed by the Reconstruction of the -Boron (111) Surface. *Phys. Rev. Lett.* **136101,** 1–6 (2013).

79. Feng, B. *et al.* Experimental Realization of Two-Dimensional Boron Sheets. *Nat. Chem.* **8,** 563–568 (2015).

80. Das, S. K., Bedar, A., Kannan, A. & Jasuja, K. Aqueous dispersions of few-layer-thick chemically modified magnesium diboride nanosheets by ultrasonication assisted exfoliation. *Sci. Rep.* **5,** 10522 (2015).

81. Gunda, H., Das, S. K. & Jasuja, K. Simple , green and high-yield production of boron based nanostructures with diverse morphologies by dissolution and recrystallization of layered magnesium diboride crystals in water. *ChemPhysChem* (2018). doi:10.1002/cphc.201701033

82. Nishino, H. *et al.* Formation Mechanism of Boron-Based Nanosheet through the Reaction of MgB2 with Water. *J. Phys. Chem. C* **121,** 10587–10593 (2017).

83. Nishino, H. *et al.* Formation and Characterization of Hydrogen Boride Sheets Derived from MgB2 by Cation Exchange. *J. Am. Chem. Soc.* **139,** 13761–13769 (2017).

84. Lim, C. S., Sofer, Z., Mazánek, V. & Pumera, M. Layered titanium diboride: towards exfoliation and electrochemical applications. *Nanoscale* **7,** 12527–12534 (2015).

85. Li, W. L. *et al.* The B35 cluster with a double-hexagonal vacancy: A new and more flexible structural motif for borophene. *J. Am. Chem. Soc.* **136,** 12257–12260 (2014).

86. Ciuparu, D., Klie, R. F., Zhu, Y. & Pfefferle, L. Synthesis of Pure Boron Single-Wall Nanotubes. *J. Phys. Chem. B* **108,** 3967–3969 (2004).

87. Zhai, H.-J. *et al.* Observation of an all-boron fullerene. *Nat. Chem.* **6,** 727–31 (2014).

88. Liu, H., Gao, J. & Zhao, J. From Boron Cluster to Two-Dimensional Mechanism and Hole Formation. *Sci. Rep.* **3,** (2013).

89. Piazza, Z. a *et al.* Planar hexagonal B(36) as a potential basis for extended single-atom layer boron sheets. *Nat. Commun.* **5,** 1–6 (2014).

90. Liu, Y., Penev, E. S. & Yakobson, B. I. Probing the Synthesis of Two-Dimensional Boron by First-Principles Computations. *Angew. Chemie Int.* **52,** 3156–3159 (2013).

91. Hernandez, Y. *et al.* High-yield production of graphene by liquid-phase exfoliation of graphite. *Nat. Nanotechnol.* **3,** 563–568 (2008).

92. Green, A. A. & Hersam, M. C. Solution Phase Production of Graphene with Controlled Thickness via Density Differentiation. *Nano Lett.* **9,** 4031–4036 (2009).

93. Behabtu, N. *et al.* Spontaneous high-concentration dispersions and liquid crystals of graphene. *Nat. Nanotechnol.* **5,** 406–411 (2010).

94. O'Neill, A., Khan, U. & Coleman, J. N. Preparation of high concentration dispersions of exfoliated MoS 2 with increased flake size. *Chem. Mater.* **24,** 2414–2421 (2012).

95. Khan, U. *et al.* Polymer reinforcement using liquid-exfoliated boron nitride nanosheets. *Nanoscale* **5,** 581–7 (2013).

96. Acerce, M., Voiry, D. & Chhowalla, M. Metallic 1T phase MoS2 nanosheets as supercapacitor electrode materials. *Nat. Nanotechnol.* **10,** 313–8 (2015).

97. Gao, M., Chan, M. K. Y. & Sun, Y. Edge-terminated molybdenum disulfide with a 9.4-Å interlayer spacing for electrochemical hydrogen production. *Nat. Commun.* **6,** 1–8 (2015).

98. Zhao, F. *et al.* Study on Thermodynamics and Kinetics for the Reaction of Magnesium Diboride and Water by Microcalorimetry. *Am. J. Anal. Chem.* **2,** 270–275 (2011).

99. Zhang, X., Luo, X., Han, J., Li, J. & Han, W. Electronic structure , elasticity and hardness of diborides of zirconium and hafnium : First principles calculations. *Comput. Mater. Sci.* **44,** 411–421 (2008).

100. Lotya, M., King, P. J., Khan, U., De, S. & Coleman, J. N. High-concentration, surfactant-stabilized graphene dispersions. *ACS Nano* **4,** 3155–3162 (2010).

101. Khan, U., Neill, A. O., Lotya, M., De, S. & Coleman, J. N. High-Concentration Solvent Exfoliation of Graphene. *Small* **6,** 864–871 (2010).

102. Garvie, L. A. J., Craven, A. J. & Brydson, R. Parallel electron energy-loss spectroscopy (PEELS) study of B in minerals: the electron energy-loss near-edge

structure (ELNES) of the B K edge. *Am. Mineral.* **80,** 1132–1144 (1995).

103. Yang, Y. & Egerton, R. F. Measurements of oscillator strength for use in elemental analysis. *Philos. Mag. Part B* **66,** 697–709 (1992).

104. Monteverde, F., Bellosi, A. & Scatteia, L. Processing and properties of ultra-high temperature ceramics for space applications. *Mater. Sci. Eng. A* **485,** 415–421 (2008).

105. Wang, Q. H. *et al.* Understanding and controlling the substrate effect on graphene electron-transfer chemistry via reactivity imprint lithography. *Nat. Chem.* **4,** 724–732 (2012).

106. Kirkland, E. J. *Advanced computing in electron microscopy*. (Springer Science & Business Media, 2010).

107. Al, B. *et al.* On the electronic and structural properties of aluminum. *J. Solid State Chem.* **177,** 389–394 (2004).

108. Mcleods, A. D., Haggerty, J. S. & Sadoway, D. R. Electrical Resistivities of Monocrystalline and Polycrystalline TiB2. *J. Am. Ceram. Soc.* **67,** 705–708 (1984).

109. C. M. Hansen. *Hansen solubility parameters: A user's handbook. CRC press* (2007).

110. Hildebrand, J. H., Prausnitz, J. M. & Scott, R. L. *Regular and related solutions: the solubility of gases, liquids, and solids*. (Van Nostrand Reinhold Co., 1970).

111. Eda, G. *et al.* Photoluminescence from chemically exfoliated MoS2. *Nano Lett.* **11,** 5111–5116 (2011).

112. Splendiani, A. *et al.* Emerging photoluminescence in monolayer MoS2. *Nano Lett.* **10,** 1271–1275 (2010).

113. Karunadasa, H. I. *et al.* A molecular MoS2 edge site mimic for catalytic hydrogen generation. *Science.* **335,** 698–702 (2012).

114. Georgakilas, V. *et al.* Functionalization of graphene: covalent and non-covalent approaches, derivatives and applications. *Chem. Rev.* **112,** 6156–6214 (2012).

115. Strano, M. S. *et al.* Electronic structure control of single-walled carbon nanotube functionalization. *Science.* **301,** 1519–1522 (2003).

116. Kuila, T. *et al.* Chemical functionalization of graphene and its applications. *Prog. Mater. Sci.* **57,** 1061–1105 (2012).

117. Englert, J. M. *et al.* Covalent bulk functionalization of graphene. *Nat. Chem.* **3,** 279 (2011).

118. Guo, B., Fang, L., Zhang, B. & Gong, J. R. Graphene doping: a review. *Insciences J.* **1,** 80–89 (2011).

119. Paulus, G. L. C., Wang, Q. H. & Strano, M. S. Covalent electron transfer chemistry of graphene with diazonium salts. *Acc. Chem. Res.* **46,** 160–170 (2012).

120. Ryder, C. R. *et al.* Covalent functionalization and passivation of exfoliated black phosphorus via aryl diazonium chemistry. *Nat. Chem.* **8,** 597 (2016).

121. Nair, N., Kim, W.-J., Usrey, M. L. & Strano, M. S. A Structure− Reactivity relationship for single walled carbon nanotubes reacting with 4-hydroxybenzene diazonium salt. *J. Am. Chem. Soc.* **129,** 3946–3954 (2007).

122. Fang, M., Wang, K., Lu, H., Yang, Y. & Nutt, S. Covalent polymer functionalization of graphene nanosheets and mechanical properties of composites. *J. Mater. Chem.* **19,** 7098–7105 (2009).

123. Yang, L. *et al.* Chloride molecular doping technique on 2D materials: WS2 and MoS2. *Nano Lett.* **14,** 6275–6280 (2014).

124. Chou, S. S. *et al.* Ligand conjugation of chemically exfoliated MoS2. *J. Am. Chem. Soc.* **135,** 4584–4587 (2013).

125. Mouri, S., Miyauchi, Y. & Matsuda, K. Tunable photoluminescence of monolayer MoS2 via chemical doping. *Nano Lett.* **13,** 5944–5948 (2013).

126. Lei, S. *et al.* Surface functionalization of two-dimensional metal chalcogenides by Lewis acid–base chemistry. *Nat. Nanotechnol.* **11,** 465 (2016).

127. Knirsch, K. C. *et al.* Basal-plane functionalization of chemically exfoliated molybdenum disulfide by diazonium salts. *ACS Nano* **9,** 6018–6030 (2015).

128. Saby, C., Ortiz, B., Champagne, G. Y. & Bélanger, D. Electrochemical modification of glassy carbon electrode using aromatic diazonium salts. 1. Blocking effect of 4-nitrophenyl and 4-carboxyphenyl groups. *Langmuir* **13,** 6805–6813 (1997).

129. Green, A. A., Silver, P. A., Collins, J. J. & Yin, P. Toehold switches: de-novo-

designed regulators of gene expression. *Cell* **159,** 925–939 (2014).

130. Lu, Y. *et al.* Graphene-protein bioelectronic devices with wavelength-dependent photoresponse. *Appl. Phys. Lett.* **100,** 33110 (2012).

131. Nečas, D. & Klapetek, P. Gwyddion: an open-source software for SPM data analysis. *Open Phys.* **10,** 181–188 (2012).

132. Bahr, J. L. & Tour, J. M. Covalent chemistry of single-wall carbon nanotubes. *J. Mater. Chem.* **12,** 1952–1958 (2002).

133. Bahr, J. L. *et al.* Functionalization of carbon nanotubes by electrochemical reduction of aryl diazonium salts: a bucky paper electrode. *J. Am. Chem. Soc.* **123,** 6536–6542 (2001).

134. Hossain, M. Z., Walsh, M. A. & Hersam, M. C. Scanning tunneling microscopy, spectroscopy, and nanolithography of epitaxial graphene chemically modified with aryl moieties. *J. Am. Chem. Soc.* **132,** 15399–15403 (2010).

135. Wang, Q. H. & Hersam, M. C. Characterization and nanopatterning of organically functionalized graphene with ultrahigh vacuum scanning tunneling microscopy. *MRS Bull.* **36,** 532–542 (2011).

136. Bekyarova, E. *et al.* Chemical modification of epitaxial graphene: spontaneous grafting of aryl groups. *J. Am. Chem. Soc.* **131,** 1336–1337 (2009).

137. Niyogi, S. *et al.* Spectroscopy of covalently functionalized graphene. *Nano Lett.* **10,** 4061–4066 (2010).

138. Backes, C. *et al.* Functionalization of Liquid-Exfoliated Two-Dimensional 2H-MoS2. *Angew. Chemie Int. Ed.* **54,** 2638–2642 (2015).

139. Jin, Z. *et al.* Click chemistry on solution-dispersed graphene and monolayer CVD graphene. *Chem. Mater.* **23,** 3362–3370 (2011).

140. Liang, Y., Thorne, J. E. & Parkinson, B. A. Controlling the electronic coupling between CdSe quantum dots and thiol capping ligands via pH and ligand selection. *Langmuir* **28,** 11072–11077 (2012).

141. Teo, W. Z., Chng, E. L. K., Sofer, Z. & Pumera, M. Cytotoxicity of Exfoliated Transition-Metal Dichalcogenides (MoS2, WS2, and WSe2) is Lower Than That of Graphene and its Analogues. *Chem. Eur. J.* **20,** 9627–9632 (2014).

142. Yin, W. *et al.* High-throughput synthesis of single-layer MoS2 nanosheets as a

near-infrared photothermal-triggered drug delivery for effective cancer therapy. *ACS Nano* **8,** 6922–6933 (2014).

143. Ou, J. Z. *et al.* Ion-driven photoluminescence modulation of quasi-two-dimensional MoS2 nanoflakes for applications in biological systems. *Nano Lett.* **14,** 857–863 (2014).

144. Nam, H. *et al.* Multiple MoS 2 transistors for sensing molecule interaction kinetics. *Sci. Rep.* **5,** 10546 (2015).

145. Patolsky, F. *et al.* Electrical detection of single viruses. *Proc. Natl. Acad. Sci. U. S. A.* **101,** 14017–14022 (2004).

146. Han, M., Gao, X., Su, J. Z. & Nie, S. Quantum-dot-tagged microbeads for multiplexed optical coding of biomolecules. *Nat. Biotechnol.* **19,** 631 (2001).

147. Wassei, J. K. & Kaner, R. B. Graphene, a promising transparent conductor. *Mater. today* **13,** 52–59 (2010).

148. Wei Zhe Teo, Elaine Lay Kim Chng, Zdenek Sofer, and M. P. Cytotoxicity of Exfoliated Transition-Metal Dichalcogenides (MoS 2 , WS 2 , and WSe 2) is Lower Than That of Graphene and its Analogues. *Chem. Eur. J.* **20,** 9627–9632 (2014).

149. Ren, Q. *et al.* SnS nanosheets for efficient photothermal therapy. *New J. Chem.* **40,** 4464–4467 (2016).

150. Yin, W. *et al.* High-Throughput Synthesis of Single- Layer MoS 2 Nanosheets as a Near- Infrared Photothermal-Triggered Drug Delivery for E ff ective Cancer Therapy. *ACS Nano* **8,** 6922–6933 (2014).

151. Pan, Y., Bao, H., Sahoo, N. G., Wu, T. & Li, L. Water-Soluble Poly (N - isopropylacrylamide)– Graphene Sheets Synthesized via Click Chemistry for Drug Delivery. *Adv. Funct. Mater.* **21,** 2754–2763 (2011).

152. Xu, S., Li, D. & Wu, P. One-Pot , Facile , and Versatile Synthesis of Monolayer MoS 2 / WS 2 Quantum Dots as Bioimaging Probes and Effi cient Electrocatalysts for Hydrogen Evolution Reaction. *Adv. Funct. Mater.* **25,** 1127–1136 (2015).

153. Sun, X. *et al.* Nano-graphene oxide for cellular imaging and drug delivery. *Nano Res.* **1,** 203–212 (2008).

154. Mansukhani, N. D. *et al.* High-Concentration Aqueous Dispersions of Nanoscale 2D Materials Using Nonionic , Biocompatible Block Copolymers. *Small* **12,** 294–

300 (2015).

155. Seo, J. W. T., Green, A. A., Antaris, A. L. & Hersam, M. C. High-concentration aqueous dispersions of graphene using nonionic, biocompatible block copolymers. *J. Phys. Chem. Lett.* **2,** 1004–1008 (2011).

APPENDIX A

SUPPLEMENTARY INFORMATION FOR CHAPTER 2

Supplementary Information

Solution-Phase Production of Two-Dimensional Metal Diborides and Their Application in Polymer Reinforcement

TEM Images of MB_2

Figure A1 shows TEM images for more flakes of metal diborides dispersed in their respective solvents as described in materials and methods. These images further establish the two-dimensional nature of metal diborides.

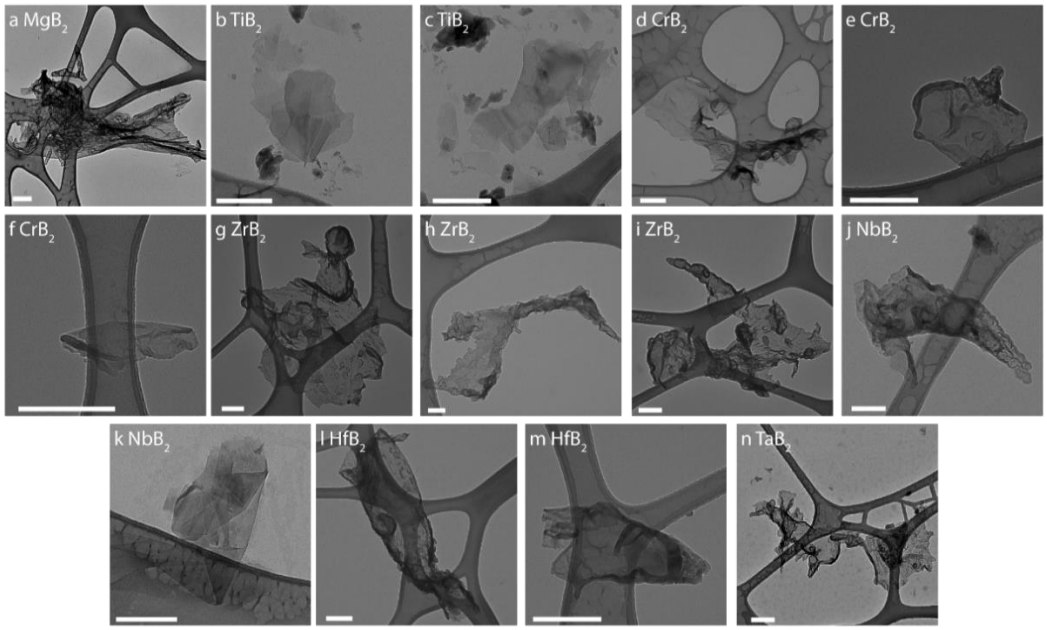

Figure A1 | TEM images of metal diborides. Low magnification TEM images of different metal borides with flake sizes ranging from 100 nm for TiB_2 to 2 μm for MgB_2. The scale bar in all images is 200 nm.

ACTEM Image of Boron Carbide

Figure A2 shows an aberration-corrected TEM image of a two-dimensional boron carbide flake with different grain boundaries which are a consequence of ultrasonication-mediated exfoliation.

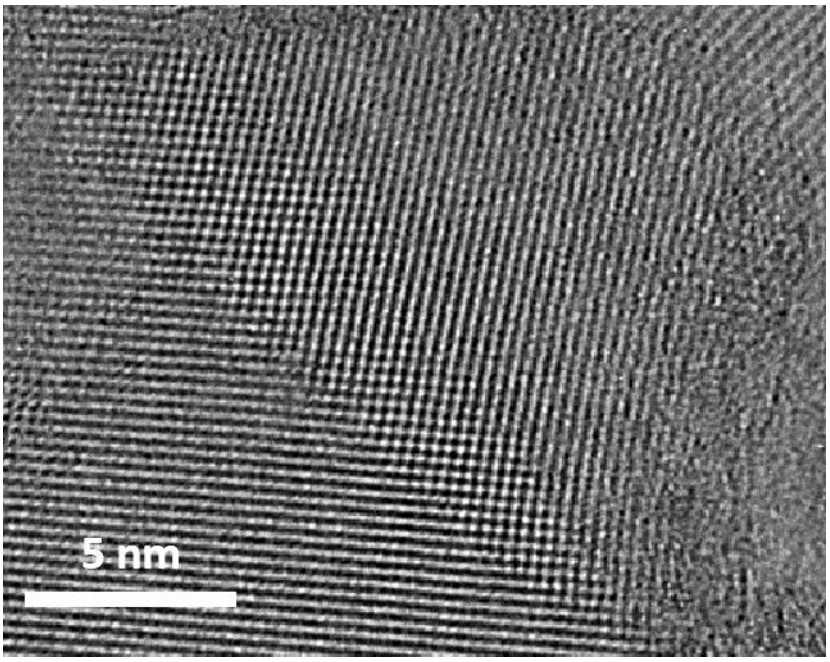

Figure A2 | ACTEM image of two-dimensional boron carbide nanosheet. The image shows different grain boundaries in the flake.

APPENDIX B

SUPPLEMENTARY INFORMATION FOR CHAPTER 4

Supplementary Information

Covalent Functionalization of Pristine Two-Dimensional Molybdenum Disulfide and Attachment of Functional Proteins

TGA curve for diazonium salt

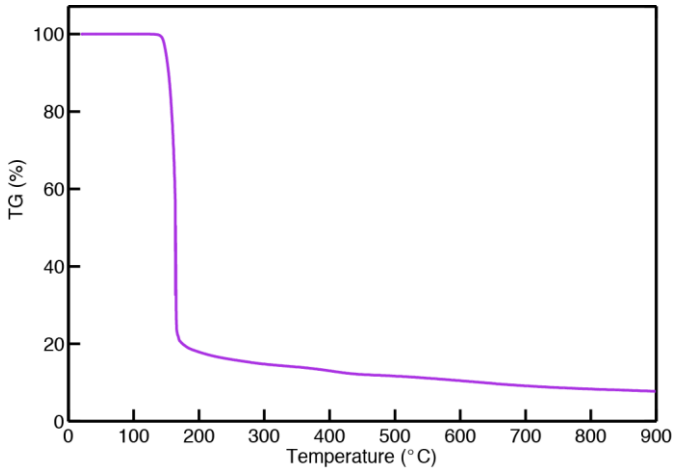

Figure B1: TGA curve for 4-nitrobenzenediazonium tetrafluoroborate salt on its own, showing significant degradation at ~160°C.

UV-vis spectra for bulk solution phased functionalized MoS_2

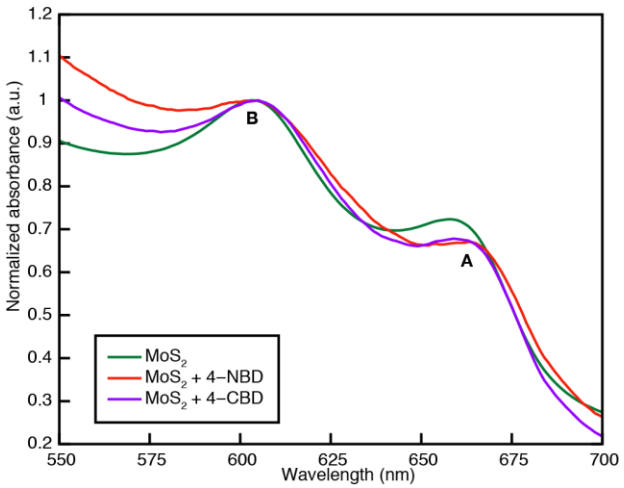

Figure B2: Absorbance spectra for MoS_2 dispersed in sodium dodecyl sulfate (SDS) (green curve), after functionalization with 4-nitrobenzenediazonium (4-NBD) tetrafluoroborate (red curve), and after functionalization with 4-carboxybenzenediazonium (4-CBD) tetrafluoroborate (purple curve).

APPENDIX C

CO-AUTHOR APPROVAL

I verify that following co-authors have approved of my use of our publications in my dissertation.

Alexander A. Green

Qing Hua Wang

Elton J. G. Santos

Ximo S. Chu

Duo O. Li

Abhishek Debnath

Anli A. Tang

Duo Ma

Matthew Gilliam

Shery Chang

Fraaz Tahir